

# *Swift* observations of the very intense flaring activity of Mrk 421 during 2006: I. Phenomenological picture of electron acceleration and predictions for the MeV/GeV emission.

A. Tramacere<sup>1,2</sup>, P. Giommi<sup>3</sup>, M. Perri<sup>3</sup>, F. Verrecchia<sup>3</sup>, and G. Tosti<sup>4,5</sup>

<sup>1</sup> CIFS - Torino, Viale Settimio Severo 3, I-10133, Torino, Italy

<sup>2</sup> SLAC, 2575 Sand Hill Road, Menlo Park, CA 94025 USA,

<sup>3</sup> ASI Science Data Center, c/o ESRIN, via G. Galilei, I-00044 Frascati, Italy

<sup>4</sup> Dipartimento di Fisica, Via A. Pascoli, I-06100 Perugia, Italy

<sup>5</sup> INFN Perugia, Via A. Pascoli, I-06100 Perugia, Italy

Received ....; accepted ....

## ABSTRACT

**Aims.** We present results from a deep spectral analysis of all the *Swift* observations of Mrk 421 from April 2006 to July 2006, when it reached its largest X-ray flux recorded until 2006. The peak flux was about 85 milli-Crab in the 2.0-10.0 keV band, with the peak energy ( $E_p$ ) of the spectral energy distribution (SED) laying often at energies larger than 10 keV. We study the trends among spectral parameters, and their physical insights in order to understand the underlying acceleration and emission mechanisms.

**Methods.** We performed spectral analysis of the *Swift* observations investigating the trends of the spectral parameters in terms of acceleration and energetic features phenomenologically linked to the SSC model parameters, predicting their effects in the  $\gamma$ -ray band, in particular the spectral shape expected in the Fermi Gamma-ray Space Telescope-*LAT* band.

**Results.** We confirm that the X-ray spectrum is well described by a log-parabolic distribution close to  $E_p$ , with the peak flux of the SED ( $S_p$ ) being correlated with  $E_p$ , and  $E_p$  anti-correlated with the curvature parameter ( $b$ ). The spectral evolution in the Hardness-ratio-flux plane shows both clock-wise and counter-clock-wise patterns. During the most energetic flares the UV-to-soft-X-ray spectral shape requires an electron distribution spectral index  $s \approx 2.3$ .

**Conclusions.** Present analysis shows that the UV-to-X-ray emission from Mrk 421 is likely to be originated by a population of electrons that is actually curved, with a low energy power-law tail. The observed spectral curvature is consistent both with stochastic acceleration or energy dependent acceleration probability mechanisms, whereas the power-law slope from *XRT-UVOT* data is very close to that inferred from the GRBs X-ray afterglow and in agreement with the *universal* first-order relativistic shock acceleration models. This scenario hints that the magnetic turbulence may play a twofold role: spatial diffusion relevant to the first order process and momentum diffusion relevant to the second order process.

**Key words.** galaxies: active - galaxies: BL Lacertae objects:individual: Mrk 421 - X-rays:individual: Mrk 421 - radiation mechanisms: non-thermal - Acceleration of particles

## 1. Introduction

BL Lac objects are Active Galactic Nuclei (AGNs) characterized by a polarised and highly variable nonthermal continuum emission extending from radio to  $\gamma$ -rays. In the most accepted scenario this radiation is produced within a relativistic jet originated by the central engine and pointing close to our line of sight. The relativistic outflow has a typical bulk Lorentz factor  $\Gamma \approx 10$ , hence the emitted fluxes, observed at an angle  $\theta$ , are subjected to the effects of a beaming factor  $\delta = 1/(\Gamma(1 - \beta \cos \theta))$ .

The Spectral Energy Distribution (SED) of these objects has a typical two-bump shape. According to current models, the lower-frequency bump is interpreted as synchrotron emission from highly relativistic electrons with Lorentz factors  $\gamma$  in excess of  $10^2$ . This component peaks at frequencies ranging from the IR to the X-ray band. The actual position of this peak has been suggested by Padovani & Giommi (1995) as a marker for a classification; they define LBL (Low energy peaked BL Lac) the objects with the first bump in the IR-to-optical band, and HBL (High energy peaked BL Lac) those peaking in the UV-X-ray band. According to the Synchrotron Self Compton (SSC) emission mechanism, the higher-frequency bump is to be attributed to inverse Compton scattering of syn-

**Table 1.** *Swift* observation journal and exposures of Mrk 421.

ObsId	Date	Start UT	XRT Exp	UVOT Exp	BAT Exp
	mm-dd-yy	(s)	(s)	(s)	(s)
00206476000(*)	04/22/06 (*)	04:21 AM	10329	10337	15156
00030352005	04/25/06	06:22 AM	4885	1214	4927
00030352006	04/26/06	03:29 AM	3526	878	3567
00030352007	04/26/06	10:48 PM	1328	329	1343
00030352008	06/14/06	12:21 AM	3187	788	3318
00030352009	06/15/06	11:42 AM	5427	1336	2787
00030352010	06/16/06	12:33 AM	23327	5868	23693
00030352011	06/18/06	12:52 AM	33288	32468	33671
00030352012	06/20/06	11:59 PM	15009	0	15379
00030352013	06/22/06	01:08 AM	20213	20430	0
00030352014	06/23/06	09:25 AM	7916	0	7221
00215769000(*)	06/23/06(*)	03:44 PM	1109	1049	5207
00030352015	06/24/06	01:37 AM	12944	0	13191
00030352016	06/27/06	03:17 AM	3046	0	3080
00219237000(*)	07/15/06(*)	04:54 AM	1916	1915	6224

(\*) Pointings triggered by the BAT instrument as GRBs.

chrotron photons by the same population of relativistic electrons that produce the synchrotron emission (Jones et al. 1974; Ghisellini & Maraschi 1989).

With its redshift  $z = 0.031$ , Mrk 421 is among the closest and best studied HBL. In fact, it is one of brightest BL Lac objects in the UV and in the X-ray bands, observed in  $\gamma$  rays by EGRET (Lin et al. 1992); it was also the first extragalactic source detected at TeV energies in the range 0.5-1.5 TeV by the Whipple telescopes (Punch et al. 1992; Petry et al. 1996).

The source is classified as HBL because its synchrotron emission peak ranges from a fraction of a keV to several keV. Its flux changes go along with strong spectral variations (Fossati et al. 2000a; Massaro et al. 2004) and the spectral shape generally exhibits a marked curvature, well described by a log-parabolic model (Massaro et al. 2004; Tramacere et al. 2007b).

In spring/summer 2006 Mrk 421 reached its largest X-ray flux recorded until that time. The peak flux was about 85 milli-Crab in the 2.0-10.0 keV band, with the peak energy of the spectral energy distribution (SED) often lying at energies larger than 10 keV.

In this paper (Paper I) we present data collected from *Swift* observations performed during this very intense flaring period. We aim to study the evolution of the spectral parameters as a function of the flaring activity, and the correlations among the spectral parameters. This gives a phenomenological picture of the physical mechanism driving the observed patterns. In Paper II we will frame this scenario in the theoretical context of stochastic acceleration (Tramacere 2009).

In the phenomenological context of jets in HBLs the spectral curvature is relevant for understanding of both radiative and acceleration mechanisms. Many works in the literature have shown that the X-ray spectral shape of Mrk 421 is actually curved and described by a

log-parabolic distribution with a mildly curved and symmetric spectral shape (Fossati et al. 2000b; Tanihata et al. 2004; Massaro et al. 2004; Tramacere et al. 2007a). Massaro et al. (2004) gave an interpretation of this feature in the framework of energy dependent acceleration efficiency that naturally leads to log-parabolic spectral distributions with a possible power-law tail at lower energies. Kardashev (1962) showed that a log-parabolic distribution results from a stochastic acceleration scenario with a mono-energetic or quasi-mono energetic particle injection. Katarzyński et al. (2006) and Giebels et al. (2007) used a relativistic Maxwellian electron distribution, resulting from a stochastic acceleration process, to describe the X-ray/TeV emission of Mrk 501 and Mrk 421 respectively. Recently, Stawarz & Petrosian (2008) showed that a distribution with similar spectral properties can be obtained as a steady state energy spectra of particles undergoing momentum diffusion due to resonant interactions with turbulent MHD modes.

Tramacere et al. (2007b) suggested that the connection of the X-ray curvature with that in the emitting particles and its evolution with the source state, could be investigated as a test for the prediction of the scenarios listed above. In particular, both stochastic (Kardashev 1962) and energy-dependent acceleration mechanisms predict an anticorrelation between the curvature and the SED peak energy ( $E_p$ ).

Moreover, the pattern shown by the peak height ( $S_p$ ) of the SED as  $E_p$  moves, can trace the evolution of the parameters characterizing the energetics of the synchrotron emission, in particular the average particle energy and the number density of the emitting particles.

A crucial issue is understanding whether during the most violent flares the shape of the X-ray spectrum also can be described by a single log-parabolic spectral distribution. In fact, a typical X-ray detector shows only a slice (usually up

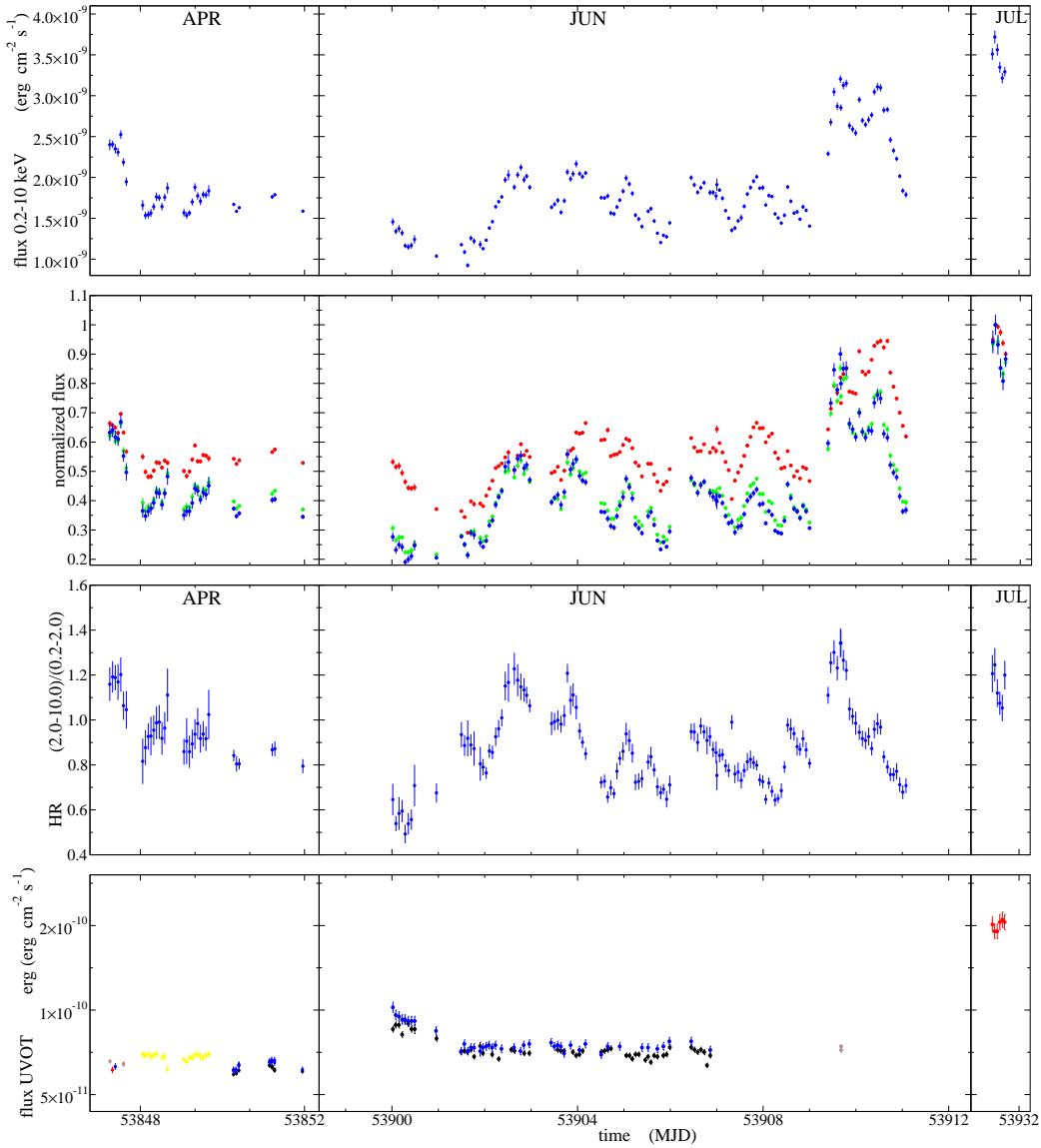


**Fig. 1.** From top to bottom: a) light curve of the flux in the band 0.2 – 10.0 keV. b) light curves for three different bands soft (0.2 – 3.0 keV, red points) medium (3.0 – 5.0 keV, green points) and hard (5.0 – 10.0 keV, blue points), normalized to their maximum value. c) the evolution of the hardness ratio (HR) evaluated as the ratio of the 2.0 – 10.0 keV band to the 0.2 – 2.0 keV band. d) light curve from the *Swift*–*UVOT* instrument, different colors refers to different filters (V=brown, U=black, UVM2=red, UVW1=blue, UVW2=yellow). [See the electronic edition of the *Journal* for a color version of this figure]

to two decades) of the overall emission from the observed object. During strong flares involving large variation of the SED peak energy, it is possible to understand if the electron distribution is curved even far from the peak energy. Moreover, we can capitalise on the unique opportunity given by *Swift* to perform simultaneous UV-to-X-ray observations, extending the spectral window from about  $10^{15}$  Hz up to  $10^{19}$  Hz. The presence of a power-law tail at low photon energies and its slope can provide information about the low-energy tail of the underlying electron distribution as well as on the acceleration mechanism generating such a spectral shape.

As final task, building on the phenomenological results from the present analysis, we can model the SED of Mrk 421 within the synchrotron-self-Compton (SSC) scenario, predicting the possible spectral behaviour at  $\gamma$ -ray energies. In particular we can relate the typical spectral shape of the UV-to-soft-X-ray emission to that expected in the MeV/GeV band covered by the Fermi Gamma-ray Space Telescope-*LAT* instrument.

This paper is organized as follows. In Sect. 2 we present our data set and the procedure used to reduce the *Swift* data. In Sect. 3 we report results from the analysis of the fast variability of the source. In section 4 we present spectral analysis results.

In section 5 we analyse the spectral evolution of the source. In Sect. 6 we study the trends among the spectral parameters and compare these results with previous studies directing our attention to the link between such trends and expectations from different scenarios for acceleration mechanism. In Sect. 7 we study the connection between the *UVOT* and the *XRT* spectra, showing the relevance of the derived spectral shape in the context of the first order acceleration processes. In sect. 8 we model the SED within the SSC framework, focusing on the phenomenological interpretation of the data. In Sect. 9 we discuss the results, and in Sect. 10 we draw our overall conclusions.

## 2. Swift Observations and data analysis

We present results from temporally-resolved spectral analyses of 15 *Swift* simultaneous observations in the UV/X-ray band performed between April and July 2006, when the source was so bright that the high-energy instrument *BAT* automatically triggered pointings at it three times assuming as if it were a Gamma Ray Burst. The log of UV/X-ray observations is reported in Tab. 1.

In Fig. 1 we report the *XRT* light curves obtained from the single-orbit spectra. In the first panel from the top we show the light curve of the flux obtained integrating the model from Eq. 2 (see section 4.2) between 0.2 and 10.0 keV, according to the parameters and parameters errors reported in Tab 2. Fluxes in Tab. 2 refer to the 0.3-10.0 keV interval because the *XRT* response function is calibrated only in that range. We extrapolated the flux to the 0.2-10.0 keV band to make easier comparisons with data from other X-ray telescopes that usually are given in the 0.2-10.0 keV band.

The second panel from the top shows the light curve for three different bands: soft (0.2 – 3.0 keV) medium (3.0 – 5.0 keV) and hard (5.0 – 10.0 keV), normalized to their maximum value. In the third panel from the top, we report the evolution of the hardness ratio (HR) evaluated as the ratio of the 2.0 – 10.0 keV band to the 0.2 – 2.0 keV band.

The bottom panel of Fig. 1 shows the light curve obtained from the *Swift-UVOT* observations.

### 2.1. *Swift-XRT* data analysis

All the data were reduced using the *XRTDAS* software (version v2.2.0) developed at the ASI Science Data Center (ASDC) and distributed within the HEASoft 6.4 package by the NASA High Energy Astrophysics Archive Research Center (HEASARC).

The operational mode of *XRT* is automatically controlled by the on-board software that uses the appropriate CCD read-out mode to reduce or eliminate the effects of photon pile-up. When the target count-rate is higher than  $\approx 1$  cts/s the system is normally operated in Windowed Timing (WT) mode whereas, the Photon Counting (PC) mode is used for fainter sources (see Burrows et al. 2005; Hill et al. 2004, for more details on *XRT* observing modes). The observations presented here were all performed in WT mode, owing to the extremely high state

of the source (40-80 cts/s).

We selected photons with grades in the range 0–2 for WT mode; we also used default screening parameters to produce level 2 cleaned event files. To take advantage of the good statistics offered by such large numbers of events we decided to make a high temporal resolved analysis, extracting spectra for each *Swift* orbit. We rejected only two out of the 174 obtained spectra, because of a strongly biased exposure. The resulting *XRT* database presented in this work therefore includes 172 time intervals.

### 2.2. *Swift-UVOT* data analysis

The *Swift* UV and Optical Telescope (*UVOT*, Roming 2005) observations included in this paper have exposures in all filters except for the White one. Photometry of the source was performed using the standard *UVOT* software developed and distributed within the HEASoft 6.4 package. Counts were extracted from an aperture of 5'' radius for all single exposures within an observation and for all filters, while the background was carefully estimated in few ways. In almost all observations the source is on the “ghost wings” (Li 2006) from the nearby star 51 UMa, so we estimated the background from a circular aperture of 15'' radius off the source but on the wings, excluding stray light and support shadows. These background values were compared to those obtained using a region outside the wings, resulting in differences in most cases within the errors.

We checked astrometry of each exposure, verifying the aperture positioning. Count rates were then converted to fluxes using the standard zero points. We discarded some exposure for which the count rate was near the limit of acceptability for the “coincidence loss” correction factor included in the CALDB ( $\sim 90$  cts  $s^{-1}$ ).

The fluxes were then de-reddened using a value for  $E(B-V)$  of 0.014 mag (Schlegel et al. 1998) with  $A_\lambda/E(B-V)$  ratios calculated for *UVOT* filters (for the latest effective wavelengths) using the mean Galactic interstellar extinction curve from Fitzpatrick (1999).

### 2.3. *Swift-BAT* data analysis

We analysed the data that automatically triggered the *BAT* instrument (labeled with \*) in Tab. 1). To reduce the data we followed the instructions reported in the *BAT* analysis threads <http://swift.gsfc.nasa.gov/docs/swift/analysis/threads/batspectrumthread.html>. We first generated a detector plane image (DPI) and checked for *noisy* pixels using the *bathotpix* task. In order to properly subtract the background we generated a weighting mask using the *batmaskwtevt* task. The spectrum was extracted using the *batbinevt* task. We applied geometric corrections (*batupdatephakw*), and systematic error correction (*batphasyserr*). As final task we generated a response matrix (*batdrngen*). The spectrum was rebinned by providing an external bin edges file to *batbinevt*.

### 3. Fast source variability.

Temporal variability is one of the most interesting features characterizing HBLs. In the X-ray band typical time scales for flux changes decrease to the order of hour or minutes. The identification of the order of the fastest significant flux change allows to estimate the source size, given by the well-known relation:

$$R \leq \frac{c \Delta t \delta}{1+z}, \quad (1)$$

where  $c$  is the speed of the light,  $\delta$  the beaming factor, and  $z$  the cosmological redshift. We investigated the intra-orbit light curves from our data set and found a significant flux variation in the first orbit on 04/26/2006 (ObsID 00030352006) pointing (see Fig. 2). The light curve extracted from the 0.3 – 10.0 keV band shows an increasing trend spanning about 1200 seconds with a variation of about 35%.

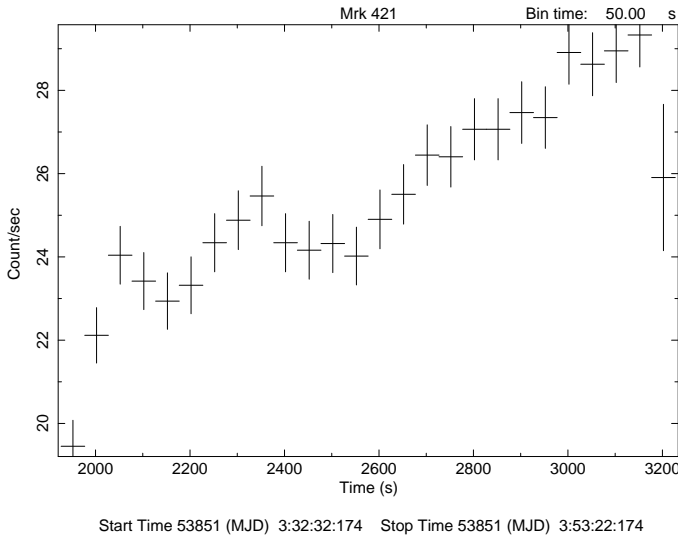


**Fig. 2.** Light curve binned with 50 s intervals, from the first orbit of the 26/04/2006 pointing. Significant variability ( $\approx 35\%$ ) is detected over intra-orbit time scale (1200 s).

According to Eq. 1, a 1200 s time scale implies  $R \leq 3.6 \times 10^{13} \delta$  cm. Assuming a beaming factor of the order of 10 we get  $R \approx 4 \times 10^{14}$  cm, which indicates a quite compact emitting region.

Lichti *et al.* (2008) analysed the temporal variability of Mrk 421 using observations performed by the *INTEGRAL-ISGR1* instrument in the 40 – 100 keV band, and overlapping our data set during the June pointings. The fastest variability observed in the *INTEGRAL-ISGR1* light curves, estimated by fitting the data with a rise-time law of the form  $a \cdot e^{t/t_0}$ , gives  $R \leq 3 \times 10^{14} \delta$  cm. We perform the same analysis for the 04/26/2006 light curve and we find  $t_0 \approx 4.100$  s which implies  $R \leq 1 \times 10^{14} \delta$  cm. We use this time scale to constrain the emitting region size in the following analyses (Sect. 8).

Time scales similar to that in the 04/26/2006 pointing were also observed by Tanihata *et al.* (2001) in *ASCA* data, about 5 ks ( $R \leq 1.5 \times 10^{14} \delta$  cm), and by Giebels *et al.* (2007) (about 2 ks

analysing TeV data from the CAT telescope ( $R \lesssim 5.4 \times 10^{13} \delta$  cm).

## 4. Spectral analysis

### 4.1. XRT spectral analysis

We find, for most of the spectra in our sample, systematic deviations (see Fig. 3) in the residuals obtained when fitting the data by means of a power-law spectrum with  $N_H$  fixed at the Galactic value. Such a behaviour heuristically suggests that the spectra are intrinsically curved. This was already known in the literature (Fossati *et al.* 2000b; Tanihata *et al.* 2004; Massaro *et al.* 2004; Tramacere *et al.* 2007a,b). All these authors agreed that when the spectral shape of Mrk 421 is curved, describing the curvature only in terms of absorption not only would require a column density much higher than the Galactic value  $N_H = 1.61 \times 10^{20} \text{cm}^{-2}$  (Lockman & Savage 1995), but also would yield in any case unacceptable fits with very high  $\chi^2_r$ . Moreover, high resolution images of the host early-type galaxy of Mrk 421 do not show in the brightness profile any evidence of large amounts of absorbing material (Urry *et al.* 2000). Based on these phenomenological results, we performed the spectral analysis fixing the  $N_H$  absorbing column densities to the Galactic values and using the following log-parabolic spectral law (LP):

$$F(E) = K E^{-(a+b \log(E))} \quad \text{ph cm}^{-2} \text{ s}^{-1} \text{ keV}^{-1}, \quad (2)$$

where  $a$  is the photon index at 1 keV and  $b$  measures the spectral curvature.

The SED peak energy ( $E_p$ ) and the SED height ( $S_p$ ) can be derived easily from Eq. 2, but in this case they suffer in intrinsic analytical correlation. This bias can be removed using an equivalent functional relationship that is a log-parabola expressed in terms of  $E_p$ ,  $S_p$  and  $b$  (LPEP):

$$S(E) = (1.60 \times 10^{-9}) S_p 10^{-b (\log(E/E_p))^2} \quad \text{erg cm}^{-2} \text{ s}^{-1}, \quad (3)$$

where  $S_p = E_p^2 F(E_p)$  and  $E_p$  are estimated during the fit, and the numerical constant is simply the energy conversion factor from keV to erg.

### 4.2. Orbit resolved analysis

Because of the very bright state of the source, we were able to extract spectra for each orbit, for a total of 172 spectra. A motivation to perform an orbit resolved analysis is the strong variability of the source during these pointings. In fact, integrating spectra over time scales much longer than the typical variability leads to misleading results in the estimates of the curvature,  $E_p$ , and  $S_p$ .

The results of the spectral analysis are reported in Tab. 2 (rejected spectra are labeled with (\*)), where all statistical errors refer to the 68% confidence level (one Gaussian

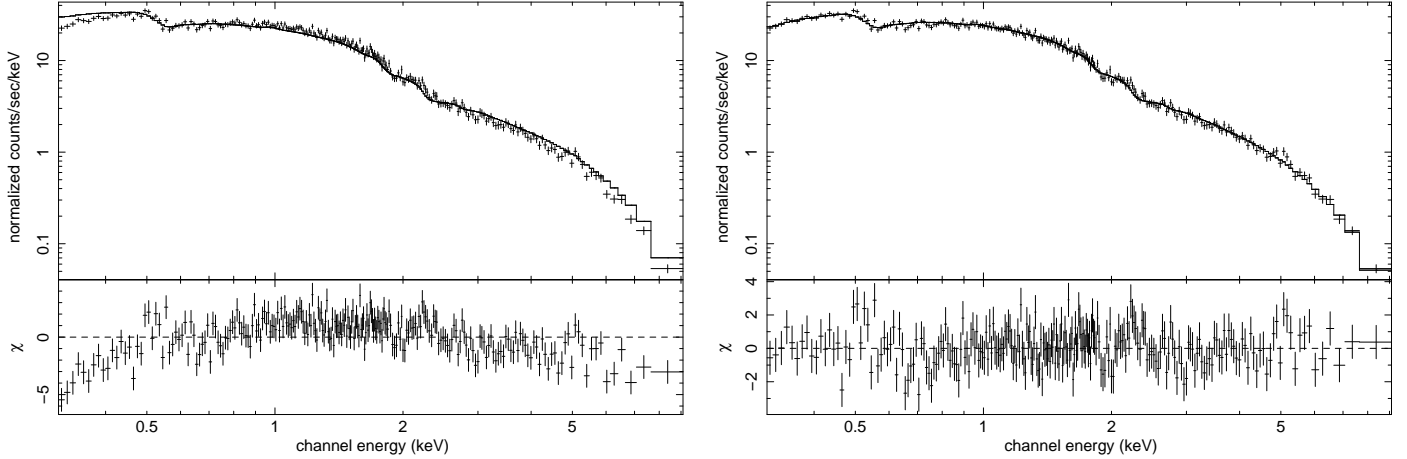


**Fig. 3.** Spectrum from the first orbit of the ObsID 00030352013 performed on 06/22/2006. *Left Panel:* the systematic deviations on both sides of the residuals from a best fit with a power-law with Galactic  $N_{\text{H}}$  show the need of intrinsic curvature. *Right Panel:* the deviations disappear with the log-parabolic model with Galactic  $N_{\text{H}}$ . The  $\chi_r^2$  decreases from 1.60 with 246 d.o.f. (power-law) to 1.19 with 245 d.o.f. (log-parabola); the F-test statistics clearly favours the curved model.

standard deviation). The second through fourth columns in Tab. 2 report the best fit estimates for the model in Eq. 2. The fifth column reports the value of the SED peak analytically estimated from Eq. 2 according to the best fit results ( $E_{p^*}$ ). The sixth and seventh columns report the  $E_p$  and  $S_p$  best fit estimates using as fitting model Eq. 3. In the eighth column we report the flux in the 0.3–10.0 keV band, evaluated by X-spec integrating the Eq. 2 model. In the last column we report the reduced  $\chi^2$  statistics for the fit with Eq. 2.

The SED peak energy was often difficult to estimate. The reason was that during this particular high brightness state, the spectra were in some cases very hard, with a photon index  $a \simeq [1.6 - 1.7]$  and having a low spectral curvature, implying a peak energy placed far out of the *XRT* energy band. In order to test the robustness of the  $E_p$  estimate, we first derived the peak energy from the spectral parameters of Eq. 2 ( $E_{p^*}$ ). Then we fitted the spectra using Eq. 3, setting the initial curvature value to that returned from the fit with Eq. 2. In order to test the stability of the results we adopted the following criteria:

1. The value of  $E_p$  statistically significant. Given the asymmetric uncertainties we define  $\sigma_{E_p}$  the half 2 sigma confidence level, and require  $E_p/\sigma_{E_p} < 1$ .
2.  $E_{p^*}$  consistent with  $E_p$  at within one sigma.

We report in Tab. 2 the estimates of  $E_p$  satisfying this criterion, in the other cases we report only the lower limit of  $E_{p^*}$ . The estimates of  $E_{p^*} > 100$  keV obviously are not statistically robust, meaning that the actual energy peak may be in excess of 100 keV, but we could not give a robust estimate. All the spectra for which the stability conditions were satisfied returned values of  $E_p \lesssim 20$  keV.

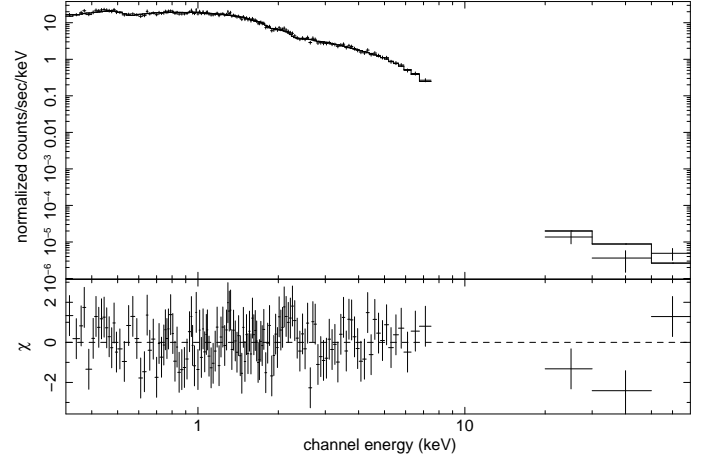


**Fig. 4.** Joint *XRT* *BAT* spectral analysis from the 04/22/2006 pointing.

### 4.3. Orbit merged analysis

The orbit resolved spectral analysis has the great advantage to follow accurately the strong variability of the source, but the  $E_p$  estimates suffer from large uncertainties. In any case, based on the spectral/flux pattern traced by the previous analysis, we can identify all the orbits indicating essentially the same spectral/flux states. We can use these intervals to perform an orbit-merged spectral analysis, to get smaller uncertainties on the  $E_p$  value, and without integrating the source over periods exhibiting large changes.

The result of this analysis is reported in Tab. 3. In this analysis when  $E_p$  and  $E_{p^*}$  can be determined the typical uncertainties are smaller. We use the values from this table to perform the  $E_p - S_p$  and  $E_p - b$  trend analysis in the following, selecting only the data with significant  $E_p$  estimates. Also in this case, all the spectra with  $E_p$  well constrained have  $E_p < 20$  keV.

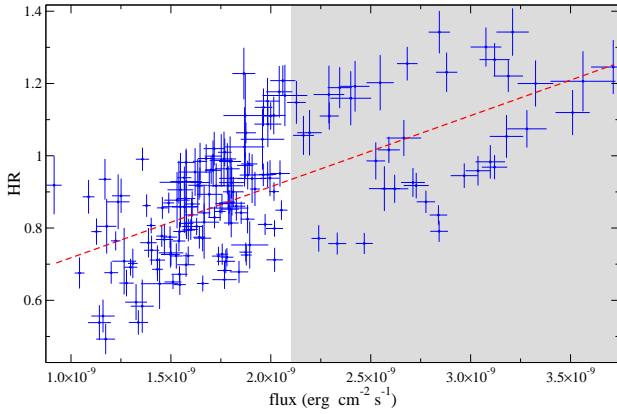


**Fig. 5.** Scatter plot of the HR vs. the flux in the 0.2–10 keV band (HR is evaluated as the ratio of the 2.0 – 10.0 keV band to the 0.2 – 2.0 keV band). The points in the shaded area are almost all from the period 06/23/2006 to 06/27/2006 and 07/15/2006.

#### 4.4. Joint XRT-BAT spectral analysis

For the three observations that have simultaneous *Swift*–*XRT* and *Swift*–*BAT* data (with the *BAT* in automatic trigger mode, see Tab. 1) we performed a joint *XRT*–*BAT* spectral analysis. The results are reported in Table 3 (lines labeled X+B). The spectral curvature resulting from the joint analysis is slightly larger with respect to the case of only *XRT* data, but is always consistent within one sigma. As already discussed, the estimation of  $E_p$  is more subtle. We will use the superscript  $X+B$  to refer to joint *XRT* and *BAT* analysis hereafter.

For the 07/15/2006 pointing, the two curvatures are  $b = 0.17 \pm 0.02$  and  $b^{X+B} = 0.20 \pm 0.02$ , and the two values of  $E_p$  consistent within one sigma are  $E_p = 11^{+4}_{-2}$  keV and  $E_p^{X+B} = 8^{+2}_{-1}$  keV. For the case of the 04/22/2006 pointing (Fig. 4), the peak energies resulting are  $E_p^{X+B} = 20^{+10}_{-6}$  keV and  $E_p = 26^{+19}_{-8}$  and the curvatures  $b = 0.11 \pm 0.02$  and  $b^{X+B} = 0.12 \pm 0.02$ .

For the 06/23/2006 pointing, the *XRT* curvature is estimated  $0.08 \pm 0.03$  to be compared to the value of  $b^{X+B} = 0.13 \pm 0.02$ . In this case the smaller value of the curvature, as discussed in the previous section, makes more difficult the estimate of the  $E_p$  value. In fact, *XRT* data are not able to locate the actual value of the peak energy, and the estimate from joint analysis is  $E_p^{X+B} = 34^{+22}_{-11}$  keV.

The results from joint *XRT*–*BAT* analysis confirm that  $E_p$  values estimated from *XRT* data, at energies larger than about 20 keV, are potentially biased. The selection applied in the present analysis should warrantee that the bias on the trends among  $E_p$ ,  $b$  and  $S_p$  will be as small as possible.

## 5. Spectral evolution

In this section we follow the classical approach of the hardness ratio (HR) analysis, to investigate cooling and/or acceleration features. The HR is evaluated as the ratio of the 2.0 – 10.0 keV band to the 0.2 – 2.0 keV band.

Analysis of the evolution of the HR shows that the correlations between variations in the soft and hard bands results in modulation of the HRs, with the spectra harder when the source is brighter and softer when weaker. This trend is clearly visible in Fig. 5. A significant scatter in the points hints that the dynamic among different flares is quite different due to different underlying physical conditions.

Moreover, we note that all but 3 of the points in the shaded area belong to the period from 06/23/2006 to 06/27/2006 and to the 07/15/2006 pointing, when the source was brighter than in the previous pointings.

A deeper understanding of the spectral dynamics can be achieved from looking at the hysteresis patterns of the single flares in the  $a$ -flux or  $HR$ -flux plane, where  $a$  is the photon index at 1 keV (see Tab. 2).

The time scales relevant to understanding the patterns in the  $a$ -flux plane are: the injection ( $\tau_{inj}$ ), the escape ( $\tau_{esc}$ ), the cooling ( $\tau_{cool}$ ), the acceleration ( $\tau_{acc}$ ) and the light crossing ( $\tau_{cross}$ ) time. According to Kirk et al. (1998), the loops are expected to be clockwise (CW) and with soft lag when the flare is observed at frequencies where the higher energy variability is faster than at lower energy. (as in the case of synchrotron cooling). On the contrary, when observed at frequencies for which the acceleration and cooling time scale are almost equal, the loops are expected to be counter-clock-wise (CCW) with a possible hard lag.

We investigated carefully all the patterns from our data-set, and in Fig. 6 and Fig. 7 we report the 5 flares showing a clear CW or CCW loop. The left panels show the evolution of  $a$  as a function of the flux, and the right panels show the light curves in three different bands. The fluxes are normalized to the maximum value reached in that particular time interval. As a general result, we did not find any significant plateau among the light curves of these flares, meaning that  $\tau_{inj} < \tau_{cross}$ . We describe the behaviour of the flares individually:

Flare 1) The flare has a CCW pattern; it begins with a softening of the spectrum with a flux almost steady (A) probably reflecting the cooling from the previous flaring episode, followed by a flux increase with a spectral hardening (B).

Flare 2) The flare has two patterns: one CW and one CCW. It starts with a decreasing flux and a spectral softening (A) ( $\tau_{cool} \ll \tau_{esc}$ ). Figure 6 (left panel) shows that the flux in the soft band is still increasing when the fluxes in the medium and hard bands are already decreasing. When the spectrum starts to get harder (B) the flux is still decreasing, this may hint that we are seeing the propagation of the new injection starting from the hard band, with the soft band still decreasing. Then, the flux starts increasing with the spectrum hardening (C). When the flare starts to decay (D) the pattern switches to CCW and we see a decrease of the flux with a spectral softening.

Flare 3) The flare has a CCW pattern. starts with a flux decrease and a spectral softening (A), then the flux increases and the spectrum hardens (B). In the last part (C), the flux decreases and the spectrum still hardens. As in the previous case this may hint the start of a new hard flaring component.

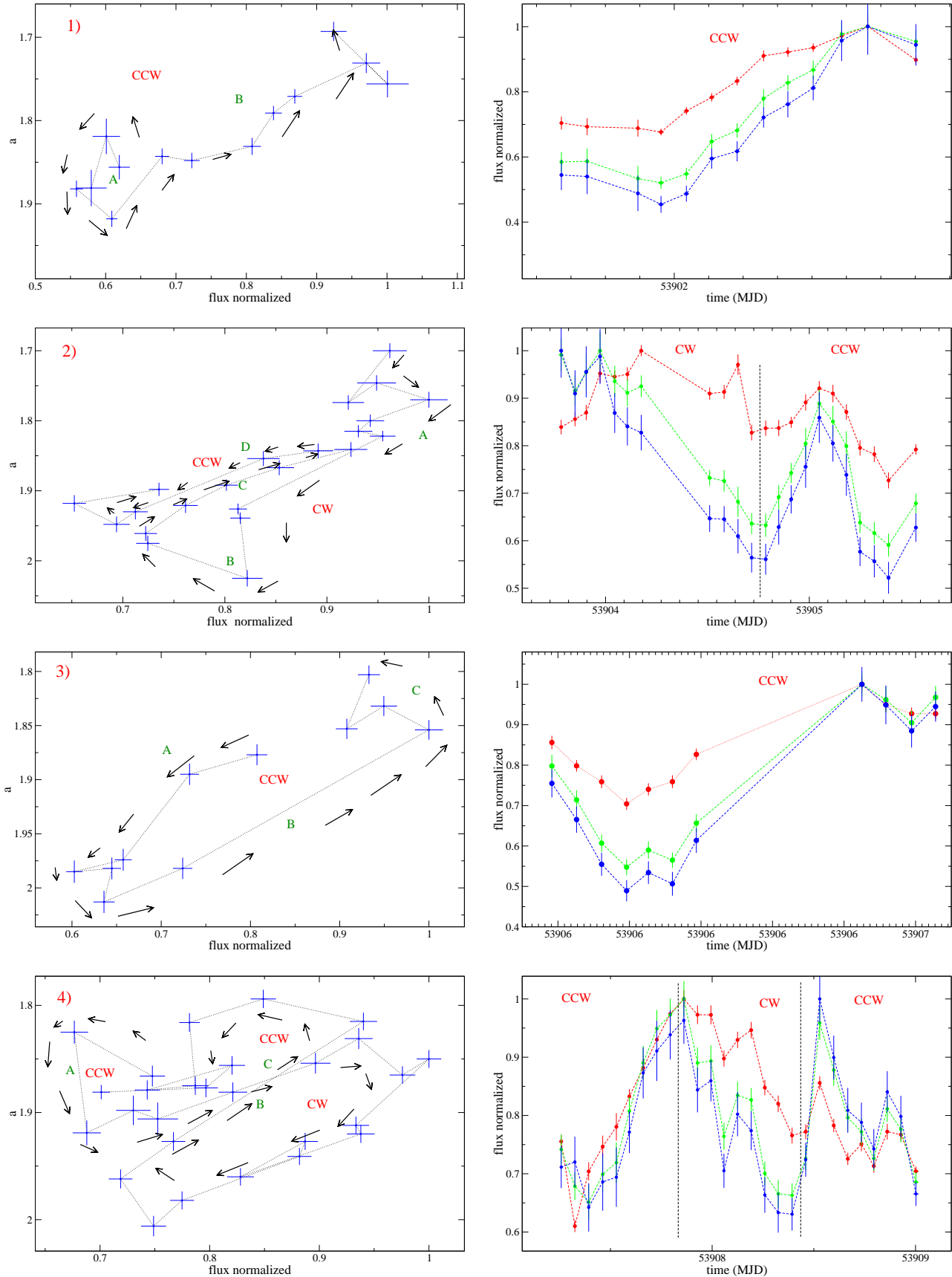


**Fig. 6.** *Left panels:* Spectral patterns in the  $a$ -flux plane showing clockwise and counterclockwise trends. *Right panels:* *Swift*-*XRT* light curves at three different bands: soft (0.2 – 3.0 keV, red), medium (3.0 – 5.0 keV, green), and hard (5.0 – 10.0 keV, red). Capital letters guide the reader during the comment in the text. In both left and right panels, the fluxes are normalized to the maximum value reached during that particular time-interval.



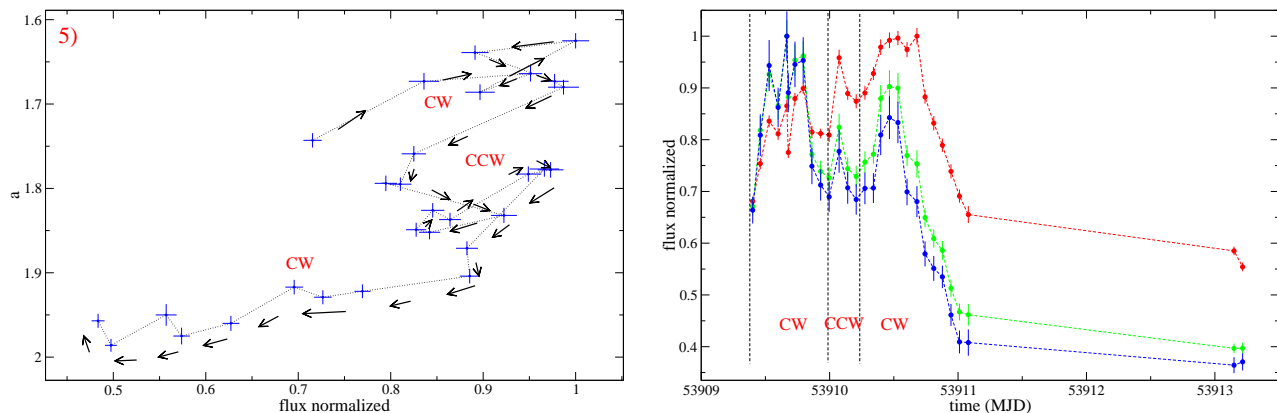


**Fig. 7.** *Left panels:* Spectral patterns in the  $a$ -flux plane showing clockwise and counterclockwise trends. *Right panels:* *Swift*-*XRT* light curves at three different bands: soft (0.2 – 3.0 keV, red), medium (3.0 – 5.0 keV, green), and hard (5.0 – 10.0 keV, red). Capital letters are referenced in the discussion in the text. In both left and right panels, the fluxes are normalized to the maximum value reached during that particular time interval.

Flare 4) This flare has three patterns: CCW, CW, and CCW. It starts with a CCW loop. Initially there is a spectral change with an almost steady flux (A), followed by a weak spectral hardening with a flux increase (B). The CW loop is dominated by the cooling time. The final CCW pattern is characterized by a flux increase and a very rapid spectral hardening. Also in this case the new flaring component seems to start from the hard band. The flux decrease (C) is almost achromatic in this case, and the escape time may be dominant over the cooling one ( $\tau_{esc} \ll \tau_{cool}$ ).

Flare 5) This flare has three patterns: CW, CCW, and CW. It does not have features different from the previous ones.

CW loops were observed for the same source in the past by Takahashi *et al.* (1996) with *ASCA* observations. Zhang (2002) observed CCW in *BeppoSAX* observations on 21 April 1998. Similar kind of loops were also observed in PKS2155-304 by Kataoka *et al.* (2000) and 1H1426+428 by Falcone *et al.* (2004).

## 6. Spectral parameter trends.

We compare the trends among the spectral parameters with those resulting from the statistical analysis in Tramacere *et al.* (2007b). We extend the data set presented in that work with the results from the observations analysed in this paper. It is worth noting that the whole data set spans about ten years, sampling the source in very different brightness states, making the final result more statistically significant.

### 6.1. $E_p - b$ trend

The evolution of the curvature parameters as a function of the peak energy points out relevant features of the acceleration process. This analysis indicates that as the peak energy of the emission increases, the cooling time scale shortens and

can compete with the time scales for acceleration. In this case, it is possible to observe a bias in the  $E_p - b$  relation, due to the cooling time scale dominating over time scales for acceleration.

We analysed the data in Tab. 3, identifying cooling-dominated observations (lines labeled with (c)), characterized by a strong flux decrease and strong spectral softening ( $a \simeq 2$ ). In Fig. 8 we plot with green empty circles the whole *XRT* data set from Tab. 3 and with black squares the points without the strong cooling contamination discussed above.

In the same figure we report also data from Tramacere *et al.* (2007b), showing that the trend in our sample is consistent with that from the historical data. This agreement confirms that the spectral curvature decreases as  $E_p$  moves toward higher energies.

This phenomenon can be interpreted according to two different scenarios. A first scenario is that of an energy-dependent acceleration probability process (EDAP). Within this context, Massaro *et al.* (2004) showed that for acceleration efficiency inversely proportional to the energy itself, the energy distribution approaches a log-parabolic shape. According to this model, the curvature ( $r$ ) is related to the fractional acceleration gain ( $\varepsilon$ ) by  $r \propto \frac{1}{\log \varepsilon}$ . A possible example is given by particles confined by a magnetic field, whose confinement efficiency ( $P_{acc}$ ) decreases as the gyration radius ( $R_L$ ) increases. From  $E_p \propto \varepsilon$  and  $r \propto \frac{1}{\log \varepsilon}$  the negative trend between  $E_p$  and  $b$  follows. This trend is in agreement with the observed trend.

An alternative explanation is provided by the stochastic acceleration framework (SA), with the presence of a momentum-diffusion term. In this scenario, the diffusion term acts on the electron spectral shape broadening the distribution. In particular, Kardashev (1962) showed that a log-parabolic spectrum results from a Fokker-Planck equation with a momentum-diffusion term and a mono-energetic or quasi-mono energetic particle injection. The results presented in Tramacere *et al.*

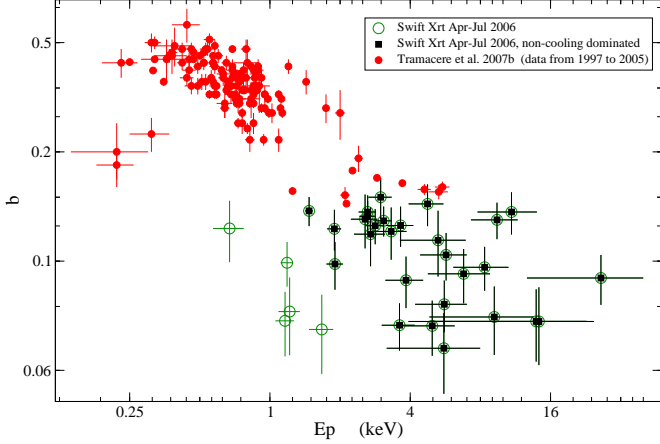


**Fig. 8.** Scatter plot of the curvature ( $b$ ) vs.  $E_p$ . Red circles represent data from Tramacere et al. (2007b) spanning from 1997 to 2005, instruments: *ASCA*, *BeppoSAX*, *XMM-Newton*. Black boxes represent *Swift* data from the present analysis without the cooling-dominated events. Empty green circles represent the whole *XRT* data set presented in this paper.

(2007b) rely on the theoretical prediction from the Kardashev (1962) model, that the curvature term ( $r$ ) is inversely proportional to the diffusion term ( $D$ ):

$$r \propto \frac{1}{Dt} . \quad (4)$$

This relation leads to the following trend among the peak energy of the electron distribution ( $\gamma_p$ ), the synchrotron curvature ( $b = r/5$ ),  $r$ , and  $E_p$ :

$$\ln(E_p) = 2 \ln(\gamma_p) + 3/(5b). \quad (5)$$

In paper II (Tramacere 2009) we will discuss in detail how the stochastic acceleration can be used to reproduce this trend drawing a physical scenario that fits this phenomenological picture. Here, we just remark that both the momentum-diffusion term  $D$  and, the fractional acceleration gain  $\varepsilon$  can explain the anticorrelation observed between  $E_p$  and  $b$ .

## 6.2. $S_p(L_p)$ - $E_p$ trend

The trend between  $S_p$  and  $E_p$  provides interesting indications concerning the driver of the spectral changes in the X-rays, in terms of the synchrotron emission. This trend can be used to understand how the luminosity of the jet evolves as the particle energy increases. In the framework of the synchrotron theory (Rybicki & Lightman 1979), the dependence of  $S_p$  on  $E_p$  can be expressed in the form of a power-law:

$$S_p \propto E_p^\alpha . \quad (6)$$

In fact, starting from the following functional relation the SED peak height reads:

$$S_p \propto n(\gamma_{3p}) \gamma_{3p}^3 B^2 \delta^4 \quad (7)$$

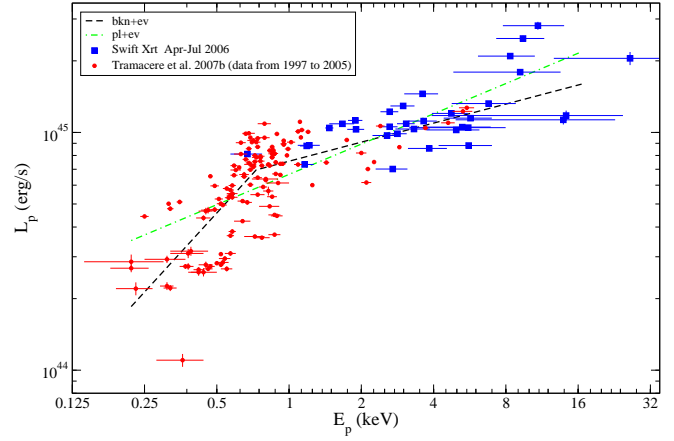


**Fig. 9.** Scatter plot of  $L_p$  vs  $E_p$ . Red circles represent data from Tramacere et al. (2007b) spanning from 1997 to 2005, instruments: *ASCA*, *BeppoSAX*, *XMM-Newton*. Blue boxes represent *Swift* data from the present analysis. The dashed dotted line represents the best fit using a power-law and the dashed line represents the best fit using a broken power law.

and the peak energy is given by:

$$E_p \propto \gamma_{3p}^2 B \delta \quad (8)$$

where  $\gamma_{3p}$  is the peak of  $n(\gamma) \gamma^3$ ,  $B$  the magnetic field, and  $\delta$  is the beaming factor.

If we take into account a log-parabolic distribution for the electrons emitting the X-ray photons, then it is easy to show that the total emitters number  $N = \int n(\gamma) d\gamma \approx n(\gamma_p) \gamma_p$ , with  $\gamma_p$  the peak of  $n(\gamma) \gamma$ . This in terms of  $S_p$  implies

$$S_p \propto N \gamma_p^2 B^2 \delta^4 . \quad (9)$$

Thus  $\alpha = 1.0$  applies when the spectral changes are dominated only by variations of the electron average energy and  $N$  is constant.  $\alpha = 1.5$  applies when the spectral changes are dominated by variations of the average electron energy but  $N$  is not constant;  $\alpha = 2$  as for changes of the magnetic field;  $\alpha = 4$  if changes in the beaming factor dominate; formally,  $\alpha = \infty$  applies for changes only in the number of emitting particles, which implies either a change in the electron density or a change in the source size. The case  $\alpha = 1.0$  holds only if the electron distribution is a log-parabola and if the curvature is constant.

In order to have a deeper understanding of the relation to the jet energetics, we plot on the y axis of Fig. 9,  $L_p = S_p 4\pi D_L^2$ , where  $D_L \approx 134.1$  Mpc is the luminosity distance<sup>1</sup>. We report the  $L_p$  values both in Tab. 2 and 3. The resulting scatter-plot represents the  $L_p - E_p$  trend obtained from merging our data sample with that from Tramacere et al. (2007b).

We fitted the data by means of a simple power law (PL)  $L_p \propto E_p^\alpha$ , and a broken power-law (BPL)

<sup>1</sup> We used a flat cosmology model with  $H_0 = 0.71$  km/(s Mpc)  $\Omega_M = 0.27$  and  $\Omega_\Lambda = 0.73$ .

$$\begin{aligned} L_p &\propto E_p^{\alpha_1}, & E_p \leq E_b \\ L_p &\propto E_p^{\alpha_2}, & E_p > E_b. \end{aligned} \quad (10)$$

The simple power-law fit gives a value of  $\alpha = 0.42 \pm 0.06$ , and the broken power law gives a break energy  $E_b = 1 \pm 1$  keV, with the two slopes  $\alpha_1 = 1.1 \pm 0.2$  and  $\alpha_2 = 0.27 \pm 0.07$ . We focus on the results from the BPL fit. Although the break energy is not well constrained, it is worth to note that spectral slopes are quite different with a high statistical significance. This break in the trend implies that for  $E_p \lesssim 1$  keV and  $L_p \lesssim 10^{45}$  erg/s the driver follows the relation with  $\alpha \simeq 1.0$  (we define this state the *quiescent* state), whilst for  $E_p \gtrsim 1$  keV and  $L_p \gtrsim 10^{45}$  erg/s, the driver is ruled by  $\alpha \simeq 0.2$  (we define this as the *high* state). In Paper II (Tramacere 2009) we will discuss in detail how the stochastic acceleration or the energetics of the jet can be used to reproduce this trend.

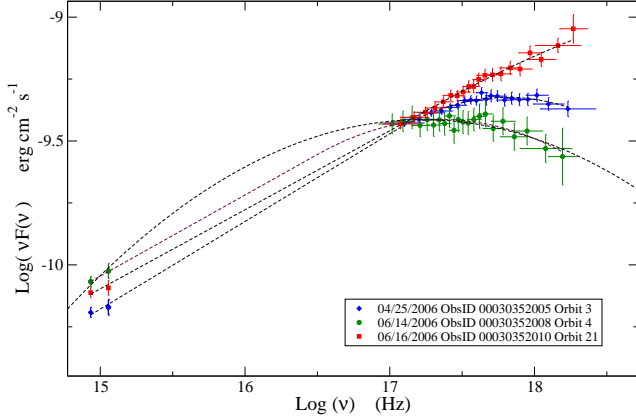


**Fig. 10.** Three different spectral shapes from the data presented in this paper. Red boxes represent a power-law spectrum observed during Orbit 3 (ObsID 00030352010) on 06/16/2006. Blue diamonds represent a spectrum that is a log-parabola with a low energy power-law tail, from Orbit 3 (ObsID 00030352005) on 04/25/2006. Green circles represent a log-parabolic spectrum from Orbit 4 (ObsID 00030352008) on 06/14/2006.

## 7. The *Swift*–*UVOT* *Swift*–*XRT* connection: the low-energy power-law tail in the electron distribution.

Both  $E_p - b$  and  $S_p - E_p$  trends allowed us to understand the shape of the electron distribution for particles emitting at energies close to  $E_p$ . Anyway, the particle energy distribution can develop a low energy shape quite different from the extrapolation of the high energy branch. This difference is relevant for discriminating among different acceleration processes. In this perspective, the connection between the UV and X-ray spectra can give useful information about the low energy tail of the

electrons emitting in the X-ray. We analysed carefully all of the spectra with simultaneous X-ray and UV observations. As result we found that joint *UVOT*–*XRT* SEDs can be classified in three categories:

- described by a log-parabola (LP)
- described by a power law (PL)
- described by a spectral law that is power law in the low energy tail, turning into a log-parabola in the high energy one (LPPL) (Massaro et al. 2006), whose functional form can be expressed by

$$\begin{aligned} \nu F(\nu) &= N (\nu/\nu_c)^{-a_\nu}, & \nu \leq \nu_c \\ \nu F(\nu) &= N (\nu/\nu_c)^{-(a_\nu+b \log(\nu/\nu_c))}, & \nu > \nu_c. \end{aligned} \quad (11)$$

where  $a_\nu$  is the spectral index of the SED ( $\nu F(\nu)$ ), and  $\nu_c$  is the frequency where happens the turn-over in the SED (Fig. 10).

From the analysis of this spectral behaviour it is possible to constrain the minimum energy of the radiating electrons. In fact electrons radiating mainly in the UV band have a Lorentz factor  $\gamma_{UV}$  satisfying the following condition (Rybicki & Lightman 1979):

$$10^{15} \text{ Hz} \simeq 3.7 \times 10^6 B \delta \gamma_{UV}^2 / (1+z) \quad (12)$$

$$\gamma_{UV} \simeq 1.6 \times 10^4 \sqrt{\frac{1+z}{B \delta}}.$$

If the spectral shape is consistent with the same log-parabola extending from the X-ray band down to the UV band (case a), then it means that electrons radiating at UV frequencies belong to the same electron population and according to Eq. 12 we have  $\gamma_{min} \lesssim \gamma_{UV}$ .

The condition  $\gamma_{min} > \gamma_{UV}$  may occur when we observe a PL (case b) or a LPPL (case c). In fact, if  $\gamma_{min} > \gamma_{UV}$  then the spectra in the X-ray-to-UV band will be described by the asymptotic low-energy approximation of the single particle synchrotron emission that is a power law with slope  $a_\nu \simeq -4/3$  ( $SED \propto \nu^{4/3}$ ) (Rybicki & Lightman 1979).

For both case b) and c) we note that our data give  $a_\nu \simeq [0.25 - 0.4]$ , a value very different from the asymptotic synchrotron kernel expectation. This hints that both cases the UV photons are likely to originate from an electron distribution that has a power law tail in the energetic range radiating in the UV-to-soft-X-ray band. A phenomenological option to explain the case c) is an electron distribution that is a power law at low energies with a log-parabolic high-energy branch (LPPL) (Massaro et al. 2006):

$$\begin{aligned} n(\gamma) &= K (\gamma/\gamma_c)^{-s}, & \gamma \leq \gamma_c \\ n(\gamma) &= K (\gamma/\gamma_c)^{-(s+r \log(\gamma/\gamma_c))}, & \gamma > \gamma_c, \end{aligned} \quad (13)$$

where  $\gamma_c$  is the turn-over energy.

In the case b), the electron distribution is assumed to be a pure power-law.

Interestingly for case b) and case c) we can also constrain the typical slope of the power-law branch of the electron distribution, using the well known relation between the spec-

tral index in the particle distribution  $s$  and that in the SED (Rybicki & Lightman 1979):

$$SED \propto \nu^{-a_\nu} = \nu^{-(s-3)/2}. \quad (14)$$

For the typical values of  $a_\nu$  observed in our data set, the resulting value of  $s$  is in the range  $s \approx [2.2 - 2.5]$ .

The presence of a power-law feature and the range of observed spectral indices are relevant both in the context of Fermi first-order acceleration models and from an observational point of view.

From the observational side, it is worth to remark that Waxman (1997) and Mészáros (2002), studying the the afterglow X-ray emission of  $\gamma$ -ray bursts (GRB), inferred an electron distribution index  $s \approx 2.3 \pm 0.1$ . This is very close to those found in our data, but coming from a quite different class of sources.

From a theoretical point of view, there are several works concerning relativistic shock acceleration models that start from different analytical or numerical approaches and find values of  $s \approx [2.2 - 2.4]$  (Achterberg et al. 2001; Gallant et al. 1999; Lemoine & Pelletier 2003; Blasi & Vietri 2005; Ellison & Double 2004). These values are consistent with those from our data set.

The power-law feature is also consistent with a purely stochastic scenario. Anyway, the usual limitation of the stochastic model to explain a *universal* index relies on the fine tuning required on the ratio of the acceleration time scale to the loss time ( $s \approx 1 + t_{acc}/t_{esc}$ ), in order to match the observed values. Moreover, we stress that a power-law electron distribution  $n(\gamma) \propto \gamma^{-2.3}$  is not compatible with a Maxwellian-like distribution ( $n(\gamma) \propto \gamma^2$ ) resulting from the equilibrium of SA processes without relevant particle escape.

In conclusion both case c) and b) are better explained better by a first order process. We will discuss this topic further in Sec. 9.

## 8. SED modeling and GeV/MeV predictions.

We model the SEDs of the three observations that have simultaneous *XRT*, *BAT* and *UVOT* data, using a standard one-zone SSC scenario. The only useful TeV data found in the literature are from *Whipple* observations on June 18,19, and 21 (Lichti et al. 2008). These data, almost simultaneous only with the 06/23/2006 *Swift* pointing, provide only the TeV flux, without giving a description of the spectrum. For this reason they are used only to estimate the TeV flux level during that pointing.

To have a feeling of the spectral and flux range of variability, we also plot *Swift-XRT* data from 03/31/2005 (Tramacere et al. 2007a), and some TeV SEDs representing the source in different flaring states (Albert et al. 2007; Yadav et al. 2007) (see left panel of Fig. 11).

The 2006 SEDs that we want to model have a power-law spectral dependence between the *UVOT* and *XRT* bands. As described in Sect. 7, the most generic distribution accounting

for this spectral shape is a power-law at low energy with a log-parabolic high-energy branch (Eq. 13). On the contrary, the 03/31/2005 SED can be modeled using a log-parabolic electron distribution that we express in terms of the peak energy as (LPEP):

$$n(\gamma) = K 10^{-r (\log(\gamma/\gamma_p))^2}. \quad (15)$$

Since we do not know the actual shape and flux at TeV energies (we have only an estimate of the flux at  $\approx 1$  TeV) we cannot constrain in detail the SSC model using the canonical  $B - \delta$  plane analysis (Tavecchio et al. 1998). Yet, we can still use the results reported in Sect. 3 and 7 to constrain some of the SSC parameters.

The first constraint comes from the source variability (see Sect. 3):

$$R/\delta \leq 1 \times 10^{14} \text{ cm}. \quad (16)$$

A second constraint comes from the analysis of the *UVOT* connection with the *XRT* data that gives an upper limit to  $\gamma_{min}$

$$\gamma_{min} \lesssim 1.6 \times 10^4 \sqrt{\frac{1+z}{B \delta}}. \quad (17)$$

To constrain the value of the maximum electron energy we can use the maximum energy of the synchrotron emission, taking as the corresponding energy the most energetic bin of the *BAT* detector with a significant signal ( $\approx 50$  keV)

$$\gamma_{max} \gtrsim 1.8 \times 10^6 \sqrt{\frac{1+z}{B \delta}}. \quad (18)$$

A further constraint on  $\gamma_{max}$  can be set by estimating the typical electron energy required to produce TeV photons (Bednarek & Protheroe 1999). Based on the historical data for Mrk 421, the spectrum typically reaches up to 10 TeV, and this implies

$$\gamma_{max} \gtrsim 2 \times 10^7 \frac{1+z}{\delta}. \quad (19)$$

And following Bednarek & Protheroe (1999), combining Eq. 19 and 18 we obtain an upper limit on the magnetic field:

$$B/\delta \lesssim 0.008 \text{ G}. \quad (20)$$

The best fit model was obtained by combining our numerical SSC code (Tramacere 2007) with a numerical minimizer. According to the observationally derived constraints, we fixed the value of the beaming factor at  $\delta = 25$ , the magnetic field  $B = 0.1 \text{ G}$ , the source size  $R = 2.1 \times 10^{15} \text{ cm}$ , and tuned  $\gamma_{min} = 1100$  to get the right Compton dominance, leaving  $r$ ,  $s$ ,  $\gamma_c$ ,  $\gamma_{max}$  and  $N$  as free parameters. The resulting best fit parameters are reported in Tab. 4 and 5.

In the left panels of Fig. 11 we show the best fit results for the SSC model for the 2006 data and for the 31/03/2005 pointing. In the right panels we show the corresponding electron distributions. The values of the electron curvature are consistent with those observed in the X-ray emission according to the relation  $b \approx r/5$ . The typical value of the ratio

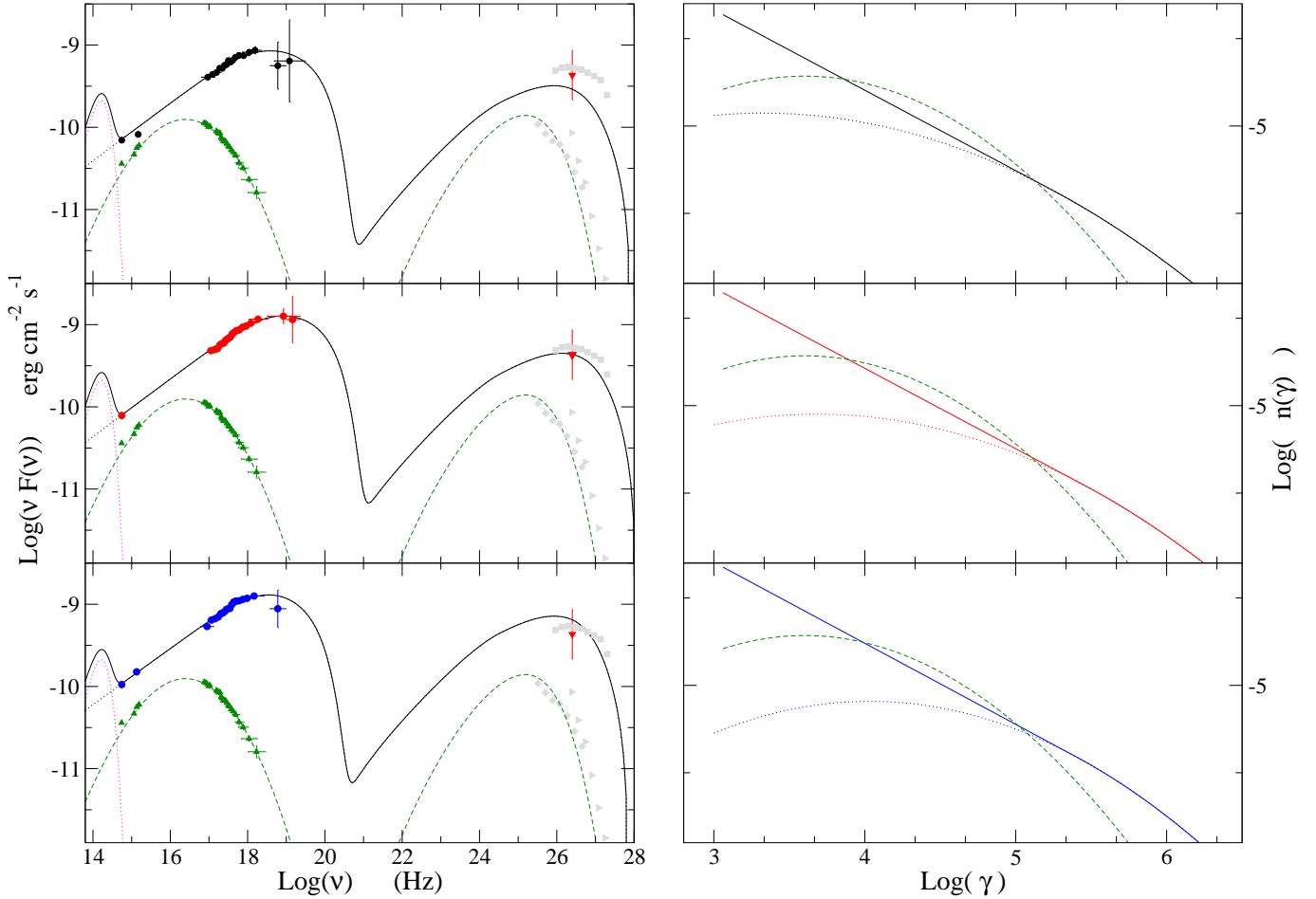


**Fig. 11.** SSC fits of three different observations with simultaneous *UVOT XRT* and *BAT* data. *Left* panels show the SSC model, from top to bottom: solid circles represent data from 04/22/2006, 06/23/2006, 07/15/2006 *Swift* observations. Green triangles show *Swift-XRT* data on 03/31/2005, data from Tramacere et al. (2007b). Solid grey polygons represent non-simultaneous EBL corrected TeV data. Solid grey squares represent the high state on 2001 observed by *Whipple*, data from Albert et al. (2007). Solid grey diamonds represent the average 2004-2005 TeV spectrum as observed by *MAGIC* (Albert et al. 2007). Solid grey right triangles represent the average spectrum from December 2005 to February 2006 as observed by *TACTIC* (Yadav et al. 2007). The solid red triangle represents a *Whipple* observation on June 18,19,21 from Lichti et al. (2008), that is very close in time to our 06/23/2006 data set. The solid lines represent the best fit by a SSC model to our simultaneous *Swift* observation, and the dashed line is the best SSC fit to the *Swift* data on 03/31/2005. The dotted lines represent the modeling of the galaxy contribution by means of black body spectral shape. *Right* panels show the electron distributions for the SSC models in the left panels. The solid lines in the right panels represent the electron distributions for the best fit models of the three 2006 *Swift* observations, the dotted lines represent the extrapolation of the LP branch of the LPPL distribution, and the dashed lines represent the electron distribution for the 03/31/2005 data.

$u_e/u_B \approx [120 - 180]$  results in a particle dominated jet in agreement with the typical values for TeV HBLs peaking in the hard X-ray (Kino et al. 2002; Sato et al. 2008). The low-energy power law branch of the electron energy distribution follows  $n(\gamma) \propto \gamma^{-2.3}$ , in agreement with the analysis presented in Sect. 7.

We remark that UV data are weakly contaminated by the host galaxy emission.

Regarding this, we plot in the left panel of Fig. 11 the contribution of the galaxy emission modeled as a black body spectral shape (dotted-line). This plot clearly shows how the

*UVOT* data taken into account lie beyond the galaxy emission spectral cut-off. On the contrary, during the low states, the possible power-law tail would lay typically at optical and lower frequencies, where the emission is typically dominated by the galaxy. This implies that we actually don't know whether the electron distribution has such a power-law tail also during the lower state. The SED model of data on 31/03/2005 shows in fact that the *UVOT* points are compatible with the synchrotron emission from a log-parabolic electron population. Moreover, a power-law low-energy branch if present in the



2005 SED would yield an index harder than those from 2006, but with much lower flux.

Another interesting analysis can be performed by looking at the acceleration time scales determined by the rate of the variation of  $E_p$ . In particular, we can use the  $e$ -folding time of  $E_p$  to infer the electron acceleration time scale  $\tau_{acc}$ . In detail, from  $E \propto \gamma^2$  it follows that the rate of change of  $E_p$  can be linked to the rate of change of  $\gamma$  for electrons radiating in the hard X-ray band. In Fig 12 we show a flare having well constrained values of  $E_p$  for the rising side. In this figure we plot the values of  $E_p$  as a function of time. The  $e$ -folding time for  $E_p$  results in a  $\gamma$   $e$ -folding time of about 0.15 days, which is the value of the typical acceleration time scale. This is the time scale that will compete with the cooling one to generate the equilibrium in the  $n(\gamma)$  distribution. In particular taking into account the synchrotron cooling:

$$\tau_{cool} \approx 10^8 / (B^2 \delta \gamma) \quad s \quad (21)$$

the equilibrium of the distribution for a log-parabolic or Maxwellian-like distribution is the peak of  $n(\gamma)$ . In the case of LPPL distribution it will be constrained between  $\gamma_c$  and  $\gamma_p^{LP}$ . Imposing  $\tau_{cool} = \tau_{acc}$  we find:

$$\gamma_{eq} = \frac{10^8}{\tau_{acc} B^2 \delta} \quad (22)$$

For  $\tau_{acc} \approx 0.15$  days,  $\delta = 25$  and using  $\gamma_{eq}$  of the order of  $10^4$  the resulting value of the magnetic field is

$$B = \sqrt{\frac{10^8}{\tau_{acc} \delta \gamma_p}} \approx 0.16 \text{ G} \quad (23)$$

which is consistent with the upper limit of Eq. 20 and with our best fit field strength.

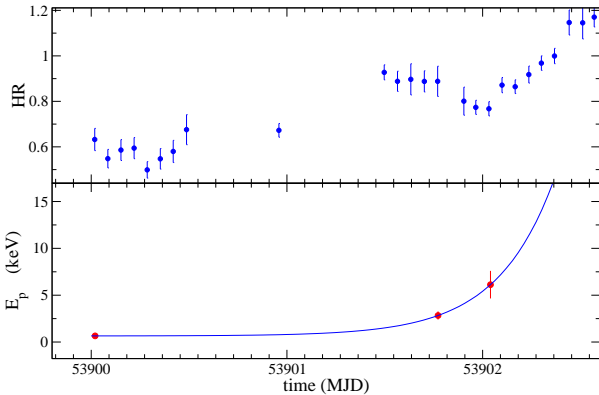


**Fig. 12.** Lower panel: the increase of  $E_p$  during a flare starting on 06/14/2006, fitted by an exponential function. Upper panel: the corresponding HR.

### 8.1. The connection between the UV slope and that at MeV/GeV energies.

A further and very relevant consequence of the spectral shape in the UV band is its connection with the shape expected at MeV/GeV energies, and in particular in the Fermi Gamma-ray Space Telescope-LAT band.

In order to explore this we simulated SSC emission accounting for a typical HBL SED. We used as the electron distribution a power-law at low energy with a log-parabolic high energy branch (LPPL) (Eq. 13). The SSC parameter are reported in the caption of Fig. 13. In the left panel of this figure we show different SEDs obtained by varying the  $s$  parameter in the range [2.1:2.5], and in the right panel we show how the spectral shape in the *UVOT* band is tightly correlated with that in the Fermi-LAT energy range. This means that a comparison between the two spectral slopes performed with simultaneous observation can hint whether actually the UV photons from the same component emitting in the X-ray are responsible for the SSC emission.

## 9. Discussion.

In this paper we presented analyses of the spectral and flux evolution of Mrk 421 during the spring/summer 2006 *Swift* observations, with the June pointings monitoring the source almost continuously for 12 days.

During this period the source exhibited both flux levels and SED peak energies at their historic maximum until 2006. This very intense flaring state of Mrk 421 represented a unique opportunity to test the correlations among the spectral parameters presented in previous works (Tramacere *et al.* 2007b), expanding the temporal spanning to about 10 years and enlarging the volume of the parameter space.

The spectral evolution of the source and the patterns in the  $a$ -flux plane (Sect. 4) suggest that each flare has a different characterization in terms of competition among the relevant time scales. Some flares showed a rise in the hard and medium X-ray band much faster than that observed in the soft X-rays. This behavior is likely to be explained with the flaring component starting in the hard X-ray band and may suggest that the driver of those flares is the rapid injection of very energetic particles rather than a gradual acceleration.

The  $S_p - E_p$  and  $E_p - b$  trends follow those presented in Tramacere *et al.* (2007b) with  $E_p$  and  $S_p$  correlated and  $E_p, b$  anti-correlated. These trends are relevant in order to understand the physical mechanisms driving the evolution of the electron distribution under the effect of acceleration processes and may represent a common scenario for HBLs. In fact, Massaro *et al.* (2008) confirmed that the  $E_p - b$  relation holds for five of the TeV HBLs included in their analysis (PKS 0548-322, 1H 1426+418, Mrk 501, 1ES 1959+650, PKS 2155-304), and that as for the  $S_p - E_p$  the only exception to the previous list is PKS 2155-304

The  $E_p - b$  relation shows a possible signature of acceleration processes leading to curved electron distributions, with

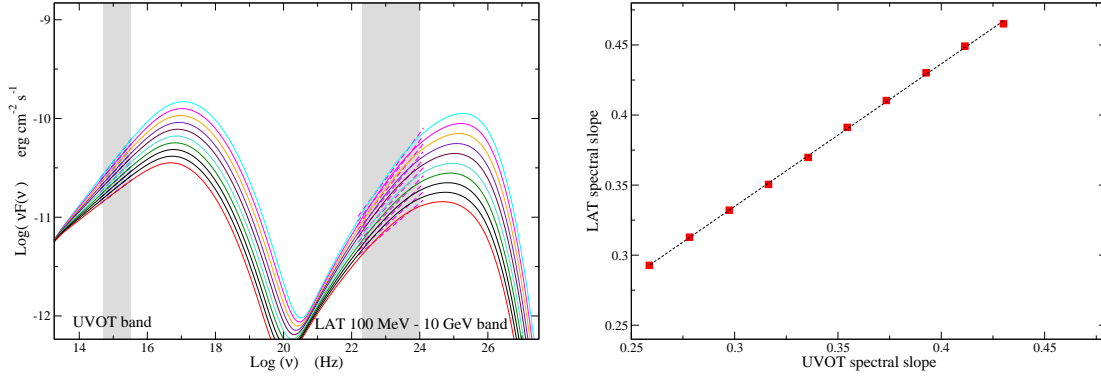


**Fig. 13.** The strong correlation between the UVOT spectral slope and that in the LAT band for a SSC scenario. In the left panel we show the SSC SEDs and in the right panel we show the correlation between the spectral slope in the *UVOT* band and that in the Fermi-LAT band. Basic parameters for the SSC model are: particle number density  $N = 10 \text{ cm}^{-3}$ , magnetic field intensity  $B = 0.1 \text{ G}$ , minimum electron energy  $\gamma_{\min} = 10^3$ , maximum electron energy  $\gamma_{\max} = 5 \times 10^6$ , emitting region radius  $R = 3.0 \times 15 \text{ cm}$ , beaming factor  $\delta = 15$ , electron curvature  $r = 1.0$ , power law of index of the low-energy tail of the electron distribution  $s = [2.2 : 2.5]$ , and turn-over energy in the electron distribution  $\gamma_c = 5.0 \times 10^4$

**Table 4.** SSC best fit results for the 2006 *Swift* observations and using as electron distribution a log-parabola with a power-law low-energy branch (Eq. 13).

Date	$B$ G	$R$ cm	$\delta$	$N(*)$ $\text{cm}^{-3}$	$r$	$s$	$\gamma_c(**)$	$\gamma_p^{LP}(***)$	$\gamma_{\max}$	$\gamma_{\min}$	$u_e/u_b$
22-04-2006	0.1	$2.1 \times 10^{15}$	25	13.5	0.75	2.30	$1.75 \times 10^5$	$2.0 \times 10^3$	$2.5 \times 10^6$	$1.1 \times 10^3$	119
23-06-2006	0.1	$2.1 \times 10^{15}$	25	15.0	0.65	2.30	$2.85 \times 10^5$	$4.8 \times 10^3$	$4.0 \times 10^6$	$1.1 \times 10^3$	135
15-07-2006	0.1	$2.1 \times 10^{15}$	25	21.0	0.85	2.32	$2.50 \times 10^5$	$1.0 \times 10^4$	$3.0 \times 10^6$	$1.1 \times 10^3$	185

**Table 5.** SSC best fit results for 31/03/2005 *Swift* observation and using a log-parabolic electron distribution as defined in Eq. 15.

Date	$B$ G	$R$ cm	$\delta$	$N(*)$ $\text{cm}^{-3}$	$r$	$\gamma_p(**)$	$\gamma_{\max}$	$\gamma_{\min}$	$u_e/u_b$
31-03-2005	0.075	$1.5 \times 10^{15}$	25	4	1.3	$4.0 \times 10^3$	$2.5 \times 10^6$	$1.1 \times 10^3$	220

(\*)  $N = \int n(\gamma) d\gamma$ .

(\*\*) Do not confuse  $\gamma_c$  (the turn-over energy in Eq. 13) with  $\gamma_p$  (the peak energy in Eq. 15).

(\*\*\*)  $\gamma_p^{LP}$  represents  $\gamma_p$  obtained from extrapolating the log-parabolic branch of the distribution described by Eq. 13. These values can be compared with  $\gamma_p$  from 31/03/2005.

the curvature decreasing as the acceleration gets more efficient. A first scenario supporting this picture is that of an energy dependent acceleration probability process (Massaro et al. 2004). An alternative explanation is provided by the stochastic acceleration framework, with the presence of a momentum-diffusion term (Kardashev 1962; Tramacere et al. 2007b). Both scenarios predict a negative correlation between  $E_p$  and  $b$  and are consistent with the data plotted in Fig. 8. It is worth noting that the data presented here substantially stretch the parameter space, confirming that the relation between the curvature and the peak energy follows the same trend from the faintest to the strongest flaring activity, hinting that the

acceleration process is actually be the same.

A future investigation may be focused on understanding which are the physical parameters that can tune the acceleration process. In this regard, an interesting investigation may be the connection of the stochastic scenario with the turbulence spectrum of the MHD waves and the resulting diffusion coefficient (Park & Petrosian 1995; Becker et al. 2006; Katarzyński et al. 2006; Stawarz & Petrosian 2008). Understanding the role of the turbulence spectrum, and in general, the role of the fluctuation on the particle energy gain, is a complex task and requires a more detailed analysis that is beyond the purpose of

this paper and will be presented in Paper II (Tramacere 2009).

The  $S_p - E_p$  trend demonstrates the connection between the average energy of the particle distribution and the power output of the source. The expected power-law dependence  $S_p \propto E_p^\alpha$  compared to the observed values of  $\alpha$ , rules out  $B, \delta$  and  $N$ , indicating  $\gamma_p$  as the main driver of the  $S_p - E_p$  trend, confirming the result from Tramacere et al. (2007b). A more detailed analysis of the scatter plot reported in Fig. 9 revealed that the trend has a break at about 1 keV, where the typical source luminosity is about  $L_p \simeq 10^{45}$  erg/s. This break may be interpreted as the marker of the competition between systematic and momentum-diffusion acceleration or in terms of energetic content of the jet. We will study such a scenario in Paper II, where we will take into account also the role  $E_p - b$  trend on  $S_p - E_p$ .

Another interesting result from our analyses is the presence a power-law tail connecting the UV data to the soft-X-ray. As explained in Sect. 7, we cannot determine whether this tail is a characteristic only of highly energetic flares, or whether it is present during low states too. The puzzling aspect in the latter case would be to reconcile a harder index with a lower flux. Anyway, if this feature is present only during strong flares then it may be argued that a relevant change has taken place in the acceleration environment. In fact, both SA and EDAP scenarios require the presence of a significant escape term to develop a power-law tail.

The value of the power-law spectral index in the electron distribution  $s \simeq 2.3$  is very close to the prediction from relativistic Fermi first order acceleration models (Achterberg et al. 2001; Gallant et al. 1999; Lemoine & Pelletier 2003; Blasi & Vietri 2005; Ellison & Double 2004) and it is similar to that found in the X-ray observations of GRB afterglows (Waxman 1997).

This observational feature, which is in nice agreement with first order acceleration models, may suggest a kind of contradiction with the results from the  $E_p - b$  trend, supporting a stochastic scenario. A more careful analysis shows that such a contradiction is only apparent. In fact, as pointed out recently by Spitkovsky (2008), diffusive shock acceleration models rely on the presence of a magnetic turbulence near the shock responsible for the scattering process, but these models do not clearly determine the possible role of the turbulence in the acceleration. The indication from our observational analysis may be simultaneous roles for the first and second order processes, with the stochastic acceleration arising from the magnetic turbulence and signed by the curvature and more generally by the  $E_p - b$  relation, and the first order signed by the slope of the electron power-law tail.

In such a circumstance the study of the curvature may offer an observational constraint for the turbulence properties, and may be recursively used to constraint the scattering process near the shock in the first order models.

We note moreover that the model presented by Spitkovsky (2008), in which the shock acceleration process is studied in a self-consistent fashion, gives results that are compatible with

our phenomenological picture. The result from this numerical study is a relativistic Maxwellian, and a high-energy tail with  $s = 2.4 \pm 0.1$ , plus an exponential cut-off moving to higher energies with time of the simulation.

This phenomenological scenario underlines the relevance of the multi-wavelength observations, and warns about the pitfalls of extrapolating the observed spectral shape over too wide a range. In this regard we stress the unique capabilities of *Swift* to perform simultaneous UV-to-X-ray observations.

A further point concerning the UV observations is given by the expected correlation of this spectral band with MeV/GeV band. In fact due to the effect of the Klein-Nishina suppression in the Inverse Compton process, we expect the UV photons to be the most efficiently up-scattered at GeV energies by the electrons radiating in the X-ray. This makes a strong correlation between the spectral slope in the UV-to-soft-X-ray band with the slope at MeV/GeV energies and in particular in the Fermi-LAT band. A test of such a correlation would be useful in order to understand whether the photons up-scattered at  $\gamma$ -ray energies are co-spatial with the electrons emitting in the X-ray.

## 10. Conclusions.

In conclusion the present work shows the complexity of the physical scenario at work in the jets of HBL objects. We have shown that the flaring activity of Mrk 421 not only causes huge flux variation but also results in complex spectral evolutions and drastic changes in the electron energy distribution. The evolution of the spectral parameters, in particular  $E_p$  and  $b$ , agrees with an acceleration model where the curvature term is inversely proportional to  $E_p$ , which is consistent with both SA and EDAP scenarios. This supports the hypothesis that the spectral curvature is related to the acceleration rather than to the cooling process. In fact we find less curved spectra as  $E_p$  increases, leading to the conclusion that the cooling is more relevant to determine the reaching of the equilibrium energy rather than to determine the spectral bending. The presence of a power-law low-energy tail remains puzzling because we cannot determine whether it develops only during strong flares or whether it is a common feature. The value  $s \simeq 2.3$  is very close to the *universal* index from relativistic shock models and could be used to understand the relative weight of the first order process during strong flares, relative to the diffusive process invoked to explain the spectral curvature. We remand these open questions to Paper II, where we will focus mainly on the theoretical interpretation of the phenomenological picture presented here.

As a final remark, we stress that as already pointed out in Massaro et al. (2006), the curvature observed in the X-ray spectra of HBLs is reflected in the TeV spectrum. The consequence is that the TeV cut-off observed in the nearby HBLs is almost entirely due to the intrinsic electron curvature rather than to the interaction with EBL photons. This scenario is therefore consistent with a low EBL density that makes the uni-



verse more transparent to high-energy radiation than previously assumed, in agreement with the discovery of HBLs objects at large redshift like H 2356-309 ( $z=0.165$ ), 1ES 1101-232 ( $z=0.186$ ) (Aharonian et al. 2006) and 1ES 128-304 ( $z=0.182$ ) (Albert et al. 2006).

*Acknowledgements.* A. Tramacere acknowledges support by a fellowship of the Italian Space Agency (ASI) and Istituto Nazionale di Astrofisica (INAF) related to the GLAST Space Mission, through the ASI/INAF I/010/06/0 contract. Gino Tosti acknowledges support by the ASI/INAF I/010/06/0 contract. We thank Dr. D. Paneque and Dr. S. Digel for useful comments.

**Table 2.** *Swift*-*XRT* Spectral analysis of Mrk 421.

Orbit	$a$	$b$	$K$	$E_{p^*}$ keV	$E_p$ keV	$S_p$ $10^{-12} \text{ erg cm}^{-2} \text{ s}^{-1}$	flux 0.3-10 keV $10^{-12} \text{ erg cm}^{-2} \text{ s}^{-1}$	$L_p$ $10^{45} \text{ erg/s}$	$\chi_r^2/\text{dof}$
<b>ObsId 00206476000 Date 4/22/2006 MJD 53847.252792</b>									
01	1.69(0.02)	0.09(0.05)	0.347(0.005)	> 10	--(- -)	--(- -)	2175.7	--(- -)	0.861(137)
02	1.66(0.02)	0.13(0.04)	0.349(0.004)	> 10	--(- -)	--(- -)	2191.2	--(- -)	1.181(197)
03	1.71(0.02)	0.07(0.04)	0.336(0.004)	> 100	--(- -)	--(- -)	2119.3	--(- -)	1.211(196)
04	1.67(0.02)	0.12(0.04)	0.334(0.004)	> 10	--(- -)	--(- -)	2093.5	--(- -)	1.224(170)
05	1.67(0.02)	0.12(0.04)	0.369(0.004)	> 10	--(- -)	--(- -)	2299.0	--(- -)	0.902(207)
06	1.7(0.02)	0.17(0.04)	0.336(0.004)	7(5)	$7_{-2}^{+5}$	727(34)	1980.1	1.56(0.07)	1.049(192)
07	1.69(0.03)	0.21(0.06)	0.306(0.005)	5(4)	$5_{-1}^{+4}$	635(32)	1761.1	1.37(0.07)	1.016(94)
08	1.86(0.03)	0.15(0.07)	0.275(0.006)	3(2)	$2.9_{-0.8}^{+3}$	475(16)	1452.2	1.02(0.03)	1.025(58)
09	1.84(0.03)	0.14(0.06)	0.25(0.004)	4(3)	$3.6_{-0.9}^{+3}$	444(14)	1347.2	0.96(0.03)	1.116(96)
10	1.79(0.03)	0.15(0.06)	0.247(0.004)	5(5)	$5_{-2}^{+6}$	465(22)	1367.5	1(0.05)	0.935(93)
11	1.82(0.03)	0.08(0.07)	0.241(0.005)	> 10	--(- -)	--(- -)	1374.0	--(- -)	1.163(80)
12	1.8(0.03)	0.08(0.06)	0.253(0.004)	> 10	--(- -)	--(- -)	1447.7	--(- -)	0.991(98)
13	1.78(0.02)	0.09(0.05)	0.269(0.004)	> 10	--(- -)	--(- -)	1562.1	--(- -)	1.020(105)
14	1.79(0.02)	0.08(0.05)	0.267(0.004)	> 10	--(- -)	--(- -)	1558.9	--(- -)	0.989(127)
15	1.83(0.02)	0.06(0.05)	0.253(0.004)	> 10	--(- -)	--(- -)	1445.0	--(- -)	1.166(119)
16	1.81(0.02)	0.07(0.05)	0.269(0.004)	> 10	--(- -)	--(- -)	1557.7	--(- -)	1.103(122)
17	1.67(0.03)	0.2(0.06)	0.285(0.005)	7(7)	$7_{-2}^{+8}$	630(47)	1691.3	1.4(0.1)	0.892(90)
18	1.85(0.03)	0.12(0.06)	0.25(0.005)	5(6)	--(- -)	--(- -)	1365.0	--(- -)	0.863(89)
19	1.81(0.03)	0.14(0.06)	0.246(0.005)	5(6)	--(- -)	--(- -)	1362.0	--(- -)	1.218(85)
20	1.83(0.02)	0.12(0.05)	0.251(0.004)	5(6)	--(- -)	--(- -)	1382.7	--(- -)	0.945(115)
21	1.81(0.02)	0.17(0.05)	0.276(0.004)	4(2)	$3.8_{-0.8}^{+2}$	502(14)	1500.4	1.08(0.03)	1.083(117)
22	1.83(0.02)	0.09(0.05)	0.294(0.004)	9(15)	--(- -)	--(- -)	1649.9	--(- -)	1.127(130)
23	1.77(0.02)	0.12(0.05)	0.275(0.004)	9(13)	--(- -)	--(- -)	1586.6	--(- -)	1.044(122)
24	1.82(0.02)	0.09(0.05)	0.267(0.004)	9(15)	--(- -)	--(- -)	1505.8	--(- -)	1.066(113)
25	1.8(0.02)	0.12(0.05)	0.283(0.004)	7(8)	$7_{-2}^{+12}$	548(34)	1589.9	1.18(0.07)	0.901(132)
26	1.8(0.02)	0.12(0.05)	0.282(0.004)	6(7)	--(- -)	--(- -)	1579.1	--(- -)	0.994(125)
27	1.74(0.03)	0.14(0.07)	0.283(0.006)	8(14)	--(- -)	--(- -)	1636.3	--(- -)	1.120(64)
<b>ObsId 00030352005 Date 4/25/2006 MJD 53850.267940</b>									
01	1.84(0.01)	0.15(0.02)	0.273(0.002)	3(1)	$3.3_{-0.4}^{+0.7}$	481(5)	1468.4	1.03(0.01)	1.360(288)
02	1.86(0.01)	0.16(0.02)	0.264(0.002)	2.7(0.7)	$2.7_{-0.3}^{+0.4}$	454(4)	1391.7	0.977(0.009)	1.248(285)
03	1.86(0.01)	0.15(0.02)	0.269(0.002)	2.9(0.8)	$2.9_{-0.3}^{+0.5}$	464(4)	1427.2	0.998(0.009)	1.090(287)
<b>ObsId 00030352006 Date 4/26/2006 MJD 53851.146539</b>									
01(*)	1.86(0.02)	0.17(0.03)	0.42(0.004)	2.5(0.7)	$2.5_{-0.3}^{+0.5}$	715(9)	2192.5	1.54(0.02)	0.989(208)
02	1.83(0.01)	0.14(0.03)	0.285(0.002)	4(2)	$4.2_{-0.8}^{+2}$	515(9)	1556.8	1.11(0.02)	1.257(253)
03	1.82(0.01)	0.17(0.03)	0.294(0.002)	3(1)	$3.4_{-0.4}^{+0.7}$	525(7)	1584.4	1.13(0.01)	1.380(254)
<b>ObsId 00030352007 Date 4/26/2006 MJD 53851.951963</b>									
01	1.87(0.01)	0.16(0.03)	0.265(0.002)	2.6(0.6)	$2.6_{-0.3}^{+0.4}$	451(4)	1388.5	0.97(0.009)	1.140(258)
<b>ObsId 00030352008 Date 6/14/2006 MJD 53900.016100</b>									
01	2(0.03)	0.12(0.07)	0.25(0.005)	1(0.2)	$1_{-0.4}^{+0.2}$	400(8)	1227.0	0.86(0.02)	0.924(178)
02	2.07(0.03)	0.14(0.06)	0.236(0.004)	0.6(0.2)	$0.6_{-0.3}^{+0.2}$	384(10)	1106.2	0.83(0.02)	1.036(173)
03	2.07(0.03)	0.05(0.07)	0.23(0.005)	0.2(0.7)	--(- -)	--(- -)	1130.2	--(- -)	0.862(171)
04	2.01(0.03)	0.2(0.07)	0.236(0.005)	0.9(0.1)	$0.9_{-0.2}^{+0.1}$	378(7)	1111.7	0.81(0.01)	1.006(175)
05	2.1(0.03)	0.2(0.06)	0.213(0.004)	0.6(0.2)	$0.6_{-0.2}^{+0.1}$	351(8)	960.3	0.76(0.02)	1.089(175)

(\*) gti with biased exposure, the affected data are not taken into account in the analyses.

The second third and fourth columns report the best fit estimate for the model in Eq. 2. The fifth column reports the value of the SED peak analytically estimated from Eq. 2 according to the best fit results. The sixth and seventh columns report the  $E_p$  and  $S_p$  best fit estimates using as best fit model Eq. 3. In the eighth column we report the flux in the 0.3-10.0 keV band, evaluated by Xspec integrating the Eq. 2 model. The ninth column reports the SED peak flux luminosity evaluated as  $L_p \simeq S_p 4\pi D_L^2$ , where  $D_L \simeq 134.1$  Mpc is the luminosity distance. In the last column we report the reduced  $\chi^2$  and the degrees of freedom concerning the Eq. 2 fit.

**Table 2.** *Swift*-*XRT* Spectral analysis of Mrk 421. *continued*

Orbit	$a$	$b$	$K$	$E_p^*$ keV	$E_p$ keV	$S_p$ $10^{-12} \text{ erg cm}^{-2} \text{ s}^{-1}$	flux 0.3-10 keV $10^{-12} \text{ erg cm}^{-2} \text{ s}^{-1}$	$L_p$ $10^{45} \text{ erg/s}$	$\chi^2/\text{dof}$
06	2.1(0.03)	0.06(0.07)	0.195(0.004)	0.2(0.5)	$0.16_{-0.07}^{+0.01}$	343(18)	939.1	0.74(0.04)	1.099(147)
07	2.08(0.03)	0.07(0.07)	0.197(0.004)	0.3(0.6)	$0.27_{-0.07}^{+0.2}$	332(14)	960.0	0.71(0.03)	0.873(143)
08	2.05(0.04)	-0.08(0.09)	0.192(0.005)	--	--(-)	--(-)	1028.5	--(-)	1.038(96)
09	2.02(0.02)	-0.01(0.04)	0.167(0.002)	--	--(-)	--(-)	872.3	--(-)	1.137(266)
<b>ObsId 00030352009 Date 6/15/2006 MJD 53901.490493</b>									
01	1.83(0.02)	0.06(0.03)	0.181(0.002)	> 10	--(-)	--(-)	1035.8	--(-)	0.979(270)
02	1.89(0.02)	-0.02(0.04)	0.162(0.002)	--	--(-)	--(-)	941.5	--(-)	1.150(219)
03	1.87(0.03)	0.01(0.06)	0.14(0.002)	> 100	--(-)	--(-)	803.3	--(-)	0.842(155)
04	1.86(0.02)	0.04(0.05)	0.194(0.003)	> 10	--(-)	--(-)	1100.3	--(-)	0.936(200)
05	1.82(0.03)	0.13(0.07)	0.196(0.004)	5(6)	--(-)	--(-)	1078.0	--(-)	0.930(111)
06	1.88(0.03)	0.11(0.07)	0.191(0.004)	4(5)	--(-)	--(-)	1021.2	--(-)	1.313(97)
07	1.88(0.01)	0.16(0.03)	0.19(0.002)	2.3(0.7)	$2.3_{-0.3}^{+0.4}$	319(4)	985.1	0.686(0.009)	1.017(273)
<b>ObsId 00030352010 Date 6/16/2006 MJD 53902.025296</b>									
01	1.92(0.01)	0.08(0.03)	0.201(0.002)	3(2)	$3.2_{-0.8}^{+2}$	337(5)	1066.9	0.73(0.01)	1.287(222)
02	1.84(0.01)	0.1(0.03)	0.219(0.002)	6(5)	$6_{-2}^{+6}$	404(13)	1213.1	0.87(0.03)	1.228(237)
03	1.85(0.01)	0.1(0.03)	0.233(0.002)	6(4)	$6_{-2}^{+5}$	425(12)	1283.5	0.91(0.02)	1.142(242)
04	1.83(0.01)	0.07(0.03)	0.254(0.003)	> 10	--(-)	--(-)	1446.7	--(-)	1.234(226)
05	1.79(0.01)	0.1(0.03)	0.263(0.002)	> 10	$12_{-5}^{+17}$	546(32)	1516.0	1.17(0.07)	1.146(263)
06	1.77(0.01)	0.1(0.03)	0.268(0.002)	> 10	$16_{-7}^{+25}$	590(43)	1574.0	1.27(0.09)	1.227(263)
07	1.73(0.02)	0.02(0.04)	0.279(0.003)	> 100	--(-)	--(-)	1773.0	--(-)	1.256(210)
08	1.76(0.02)	-0.03(0.05)	0.281(0.004)	--	--(-)	--(-)	1808.0	--(-)	0.926(111)
09(*)	1.72(0.02)	0.02(0.03)	0.427(0.004)	> 100	--(-)	--(-)	2741.8	--(-)	1.180(230)
10	1.69(0.02)	0.04(0.03)	0.261(0.003)	> 100	--(-)	--(-)	1697.5	--(-)	1.110(220)
11	1.7(0.02)	0.04(0.03)	0.285(0.003)	> 100	--(-)	--(-)	1833.8	--(-)	1.139(227)
12	1.73(0.01)	0.03(0.03)	0.302(0.003)	> 100	--(-)	--(-)	1911.1	--(-)	1.258(240)
13	1.76(0.02)	0(0.03)	0.279(0.003)	--	--(-)	--(-)	1764.0	--(-)	1.120(230)
14	1.74(0.01)	0.04(0.02)	0.29(0.002)	> 100	--(-)	--(-)	1812.6	--(-)	1.034(288)
15	1.77(0.01)	0.04(0.02)	0.277(0.002)	> 100	--(-)	--(-)	1677.1	--(-)	1.093(279)
16	1.81(0.01)	0.05(0.03)	0.246(0.002)	> 10	--(-)	--(-)	1443.2	--(-)	1.128(242)
17	1.8(0.01)	0.03(0.03)	0.248(0.002)	> 100	--(-)	--(-)	1485.6	--(-)	1.330(262)
18	1.84(0.01)	-0.05(0.03)	0.248(0.002)	--	--(-)	--(-)	1512.6	--(-)	1.049(236)
19	1.84(0.01)	-0.05(0.03)	0.225(0.002)	--	--(-)	--(-)	1383.1	--(-)	0.978(221)
20	1.81(0.01)	-0.04(0.03)	0.245(0.002)	--	--(-)	--(-)	1517.3	--(-)	1.100(241)
21	1.7(0.02)	0.03(0.03)	0.287(0.003)	> 100	--(-)	--(-)	1871.2	--(-)	1.038(240)
22	1.77(0.01)	0(0.03)	0.284(0.003)	--	--(-)	--(-)	1769.6	--(-)	1.214(234)
23	1.75(0.02)	0.03(0.03)	0.293(0.003)	> 100	--(-)	--(-)	1833.7	--(-)	1.116(226)
24	1.77(0.02)	0.05(0.03)	0.32(0.003)	> 100	--(-)	--(-)	1930.8	--(-)	1.301(215)
<b>ObsId 00030352011 Date 6/18/2006 MJD 53904.038766</b>									
01	1.8(0.01)	0.11(0.03)	0.318(0.003)	9(8)	$9_{-3}^{+8}$	633(27)	1808.8	1.36(0.06)	1.036(286)
02	1.82(0.01)	0.12(0.03)	0.319(0.003)	6(4)	$6_{-1}^{+3}$	600(15)	1777.2	1.29(0.03)	1.227(286)
03	1.82(0.01)	0.18(0.02)	0.34(0.002)	3.1(0.7)	$3.1_{-0.3}^{+0.4}$	601(6)	1817.5	1.29(0.01)	1.343(317)
04	1.93(0.01)	0.13(0.02)	0.294(0.002)	1.9(0.4)	$1.9_{-0.2}^{+0.2}$	482(4)	1511.3	1.037(0.009)	1.211(297)
05	1.94(0.01)	0.11(0.03)	0.292(0.002)	1.9(0.5)	$1.9_{-0.2}^{+0.3}$	476(4)	1507.0	1.024(0.009)	1.216(287)
06	2.03(0.02)	0.04(0.04)	0.292(0.004)	0.5(0.5)	$0.5_{-0.5}^{+0.4}$	471(24)	1482.8	1.01(0.05)	1.242(198)

(\*) gti with biased exposure, the affected data are not taken into account in the analyses.

The second third and fourth columns report the best fit estimate for the model in Eq. 2. The fifth column reports the value of the SED peak analytically estimated from Eq. 2 according to the best fit results. The sixth and seventh columns report the  $E_p$  and  $S_p$  best fit estimates using as best fit model Eq. 3. In the eighth column we report the flux in the 0.3-10.0 keV band, evaluated by Xspec integrating the Eq. 2 model. The ninth column reports the SED peak flux luminosity evaluated as  $L_p \approx S_p 4\pi D_L^2$ , where  $D_L \approx 134.1$  Mpc is the luminosity distance. In the last column we report the reduced  $\chi^2$  and the degrees of freedom concerning the Eq. 2 fit.

**Table 2.** *Swift*-*XRT* Spectral analysis of Mrk 421. *continued*

Orbit	$a$	$b$	K	$E_p^*$ keV	$E_p$ keV	$S_p$ $10^{-12} \text{ erg cm}^{-2} \text{ s}^{-1}$	flux 0.3-10 keV $10^{-12} \text{ erg cm}^{-2} \text{ s}^{-1}$	$L_p$ $10^{45} \text{ erg/s}$	$\chi_r^2/\text{dof}$
07	1.98(0.02)	0.08(0.04)	0.259(0.003)	1.5(0.5)	$1.4^{+0.4}_{-0.3}$	416(5)	1330.3	0.9(0.01)	1.002(213)
08	1.96(0.02)	0.15(0.04)	0.267(0.003)	1.4(0.2)	$1.4^{+0.1}_{-0.1}$	430(5)	1333.3	0.93(0.01)	1.199(219)
09	1.92(0.02)	0.09(0.03)	0.269(0.003)	3(2)	$2.7^{+2}_{-0.6}$	448(6)	1420.2	0.96(0.01)	1.085(230)
10	1.89(0.01)	0.06(0.03)	0.273(0.002)	9(14)	--(--)	--(--)	1501.8	--(--)	1.174(291)
11	1.87(0.02)	0.07(0.03)	0.289(0.003)	10(19)	--(--)	--(--)	1600.5	--(--)	1.178(233)
12	1.84(0.02)	0.01(0.03)	0.298(0.003)	> 100	--(--)	--(--)	1746.9	--(--)	1.016(243)
13	1.84(0.02)	0.07(0.03)	0.299(0.003)	> 10	--(--)	--(--)	1687.1	--(--)	1.122(240)
14	1.85(0.02)	0.09(0.03)	0.286(0.003)	6(7)	$6^{+10}_{-2}$	525(22)	1580.9	1.13(0.05)	1.058(233)
15	1.93(0.02)	0.11(0.03)	0.256(0.003)	2(0.7)	$2^{+0.5}_{-0.3}$	419(5)	1321.3	0.9(0.01)	1.228(222)
16	1.95(0.02)	0.1(0.04)	0.248(0.003)	1.9(0.8)	$1.9^{+0.6}_{-0.3}$	403(5)	1280.6	0.87(0.01)	1.101(210)
17	1.92(0.02)	0.14(0.04)	0.236(0.003)	2(0.6)	$1.9^{+0.4}_{-0.2}$	388(5)	1249.5	0.83(0.01)	1.274(207)
18	1.9(0.01)	0.08(0.03)	0.255(0.002)	5(5)	$5^{+6}_{-1}$	441(11)	1376.8	0.95(0.02)	1.112(254)
19	1.88(0.01)	0.07(0.03)	0.256(0.002)	7(9)	--(--)	--(--)	1409.5	--(--)	1.088(251)
20	1.9(0.01)	0.1(0.03)	0.239(0.002)	3(2)	$3.2^{+2}_{-0.7}$	407(6)	1272.2	0.88(0.01)	1.213(244)
21	1.97(0.01)	0.07(0.03)	0.218(0.002)	1.5(0.5)	$1.5^{+0.4}_{-0.3}$	350(4)	1121.5	0.753(0.009)	1.109(230)
22	1.99(0.02)	0.11(0.03)	0.204(0.002)	1.2(0.2)	$1.2^{+0.2}_{-0.2}$	328(4)	1023.7	0.706(0.009)	0.993(225)
23	1.98(0.01)	0.06(0.03)	0.212(0.002)	1.4(0.6)	$1.4^{+0.6}_{-0.3}$	340(4)	1097.1	0.732(0.009)	0.944(227)
24	2.01(0.01)	0.09(0.04)	0.215(0.002)	0.8(0.2)	$0.9^{+0.2}_{-0.2}$	344(4)	1072.8	0.74(0.009)	1.065(220)
25	1.98(0.01)	0.03(0.03)	0.234(0.002)	2(2)	--(--)	--(--)	1229.9	--(--)	1.127(235)
26	1.85(0.01)	-0.02(0.03)	0.295(0.003)	--	--(--)	--(--)	1809.2	--(--)	1.290(269)
27	1.83(0.01)	0.02(0.03)	0.285(0.003)	> 100	--(--)	--(--)	1676.1	--(--)	1.249(268)
28	1.85(0.01)	0.02(0.03)	0.276(0.003)	> 100	--(--)	--(--)	1595.7	--(--)	1.322(261)
29	1.8(0.01)	0.06(0.03)	0.285(0.002)	> 10	--(--)	--(--)	1662.8	--(--)	1.132(293)
30	1.83(0.01)	0.02(0.03)	0.29(0.002)	> 100	--(--)	--(--)	1701.8	--(--)	1.178(284)
31	1.83(0.02)	0.08(0.03)	0.401(0.004)	10(15)	--(--)	--(--)	2260.2	--(--)	1.022(237)
32	1.83(0.02)	0.08(0.03)	0.281(0.003)	> 10	--(--)	--(--)	1598.0	--(--)	0.894(231)
33	1.84(0.02)	0.11(0.04)	0.289(0.003)	6(5)	$6^{+6}_{-2}$	531(19)	1593.0	1.14(0.04)	0.876(220)
34	1.82(0.03)	0.17(0.06)	0.29(0.005)	3(2)	$3.5^{+3}_{-0.8}$	520(16)	1557.4	1.12(0.03)	1.092(101)
<b>ObsId 00030352012 Date 6/20/2006 MJD 53907.001774</b>									
01	1.92(0.03)	0.09(0.08)	0.311(0.007)	3(4)	--(--)	--(--)	1629.2	--(--)	0.853(64)
02	1.83(0.01)	0.16(0.02)	0.303(0.002)	3.4(0.9)	$3.4^{+0.6}_{-0.4}$	538(6)	1631.2	1.16(0.01)	1.179(297)
03	1.83(0.01)	0.16(0.03)	0.286(0.002)	3(1)	$3.3^{+0.7}_{-0.4}$	506(7)	1535.8	1.09(0.01)	1.065(247)
04	1.87(0.01)	0.16(0.03)	0.267(0.002)	2.6(0.8)	$2.6^{+0.5}_{-0.3}$	455(5)	1399.4	0.98(0.01)	1.113(235)
05	1.87(0.01)	0.18(0.03)	0.253(0.002)	2.3(0.6)	$2.3^{+0.3}_{-0.2}$	429(5)	1313.9	0.92(0.01)	1.163(227)
06	1.83(0.02)	-0.01(0.03)	0.198(0.002)	--	--(--)	--(--)	1191.2	--(--)	0.932(218)
07	1.92(0.02)	0.09(0.04)	0.225(0.003)	3(2)	$2.8^{+2}_{-0.7}$	376(6)	1189.5	0.81(0.01)	0.968(187)
08	1.9(0.02)	0.14(0.05)	0.244(0.003)	2(1)	$2.3^{+0.9}_{-0.4}$	408(7)	1269.1	0.88(0.01)	1.046(149)
09	1.91(0.02)	0.16(0.05)	0.255(0.004)	2(0.8)	$2^{+0.6}_{-0.3}$	422(7)	1305.3	0.91(0.01)	1.071(112)
10	1.88(0.01)	0.15(0.03)	0.275(0.002)	2.5(0.8)	$2.5^{+0.5}_{-0.3}$	464(5)	1438.3	1(0.01)	1.145(239)
11	1.85(0.01)	0.14(0.03)	0.294(0.003)	3(2)	$3.4^{+1}_{-0.6}$	514(8)	1577.8	1.11(0.02)	1.284(229)
12	1.83(0.01)	0.2(0.03)	0.316(0.003)	2.6(0.6)	$2.6^{+0.4}_{-0.2}$	548(6)	1657.9	1.18(0.01)	1.255(232)
13	1.87(0.01)	0.15(0.03)	0.325(0.003)	2.8(0.8)	$2.8^{+0.5}_{-0.3}$	556(6)	1713.4	1.2(0.01)	1.082(262)
14	1.85(0.01)	0.19(0.03)	0.337(0.003)	2.5(0.6)	$2.5^{+0.3}_{-0.2}$	578(6)	1762.0	1.24(0.01)	1.167(258)
15	1.91(0.01)	0.16(0.03)	0.319(0.003)	1.8(0.3)	$1.8^{+0.2}_{-0.1}$	524(5)	1620.8	1.13(0.01)	1.199(252)

(\*) gti with biased exposure, the affected data are not taken into account in the analyses.

The second third and fourth columns report the best fit estimate for the model in Eq. 2. The fifth column reports the value of the SED peak analytically estimated from Eq. 2 according to the best fit results. The sixth and seventh columns report the  $E_p$  and  $S_p$  best fit estimates using as best fit model Eq. 3. In the eighth column we report the flux in the 0.3-10.0 keV band, evaluated by Xspec integrating the Eq. 2 model. The ninth column reports the SED peak flux luminosity evaluated as  $L_p \simeq S_p 4\pi D_L^2$ , where  $D_L \simeq 134.1$  Mpc is the luminosity distance. In the last column we report the reduced  $\chi^2$  and the degrees of freedom concerning the Eq. 2 fit.

**Table 2.** *Swift*–*XRT* Spectral analysis of Mrk 421. *continued*

Orbit	$a$	$b$	K	$E_{p^*}$ keV	$E_p$ keV	$S_p$ $10^{-12} \text{ erg cm}^{-2} \text{ s}^{-1}$	flux 0.3–10 keV $10^{-12} \text{ erg cm}^{-2} \text{ s}^{-1}$	$L_p$ $10^{45} \text{ erg/s}$	$\chi_r^2/\text{dof}$
16	1.92(0.01)	0.14(0.03)	0.316(0.003)	2(0.5)	$2^{+0.3}_{-0.2}$	519(5)	1623.1	1.12(0.01)	1.068(246)
<b><i>ObsId 00030352013 Date 6/22/2006 MJD 53908.050644</i></b>									
01	1.96(0.01)	0.18(0.03)	0.291(0.002)	1.3(0.1)	$1.28^{+0.08}_{-0.08}$	468(4)	1424.1	1.007(0.009)	1.191(245)
02	1.93(0.01)	0.15(0.03)	0.302(0.002)	1.8(0.3)	$1.8^{+0.2}_{-0.1}$	493(4)	1537.5	1.061(0.009)	1.360(256)
03	1.94(0.01)	0.18(0.03)	0.308(0.002)	1.5(0.2)	$1.45^{+0.1}_{-0.09}$	498(4)	1522.5	1.072(0.009)	1.088(253)
04	1.98(0.01)	0.15(0.03)	0.269(0.002)	1.2(0.1)	$1.2^{+0.1}_{-0.1}$	431(4)	1323.0	0.927(0.009)	1.083(241)
05	2.01(0.01)	0.08(0.03)	0.252(0.002)	0.9(0.2)	$0.9^{+0.2}_{-0.3}$	404(4)	1268.0	0.869(0.009)	1.006(213)
06	1.96(0.01)	0.12(0.03)	0.243(0.002)	1.5(0.3)	$1.5^{+0.2}_{-0.1}$	392(4)	1231.3	0.843(0.009)	1.208(235)
07	1.93(0.01)	0.03(0.03)	0.243(0.002)	> 10	--(--)	--(--)	1322.9	--(--)	1.063(245)
08	1.82(0.01)	0.03(0.02)	0.281(0.002)	> 100	--(--)	--(--)	1667.5	--(--)	1.434(277)
09	1.79(0.01)	0.09(0.03)	0.263(0.002)	> 10	$12^{+16}_{-5}$	545(32)	1516.0	1.17(0.07)	1.163(265)
10	1.82(0.01)	0.07(0.03)	0.241(0.002)	> 10	--(--)	--(--)	1384.9	--(--)	1.275(256)
11	1.88(0.01)	0.02(0.03)	0.241(0.002)	> 100	--(--)	--(--)	1374.1	--(--)	1.247(256)
12	1.88(0.01)	0.02(0.03)	0.229(0.002)	> 100	--(--)	--(--)	1300.0	--(--)	1.051(244)
13	1.86(0.01)	0.02(0.03)	0.25(0.002)	> 100	--(--)	--(--)	1438.9	--(--)	1.036(255)
14	1.88(0.01)	0.02(0.03)	0.245(0.002)	> 100	--(--)	--(--)	1393.2	--(--)	1.221(254)
15	1.88(0.01)	0.12(0.02)	0.231(0.001)	3(1)	$3.1^{+0.7}_{-0.4}$	395(4)	1227.7	0.85(0.009)	1.334(308)
<b><i>ObsId 00030352014 Date 6/23/2006 MJD 53909.394900</i></b>									
01	1.74(0.01)	0.02(0.02)	0.326(0.003)	> 100	--(--)	--(--)	2060.1	--(--)	1.163(281)
02	1.67(0.01)	0.06(0.03)	0.372(0.003)	> 100	--(--)	--(--)	2435.1	--(--)	1.240(255)
03	1.66(0.01)	0.02(0.03)	0.411(0.004)	> 100	--(--)	--(--)	2783.6	--(--)	1.110(276)
04	1.69(0.01)	0.04(0.03)	0.398(0.003)	> 100	--(--)	--(--)	2603.6	--(--)	1.234(265)
05	1.63(0.01)	0.08(0.03)	0.436(0.004)	> 100	--(--)	--(--)	2938.2	--(--)	1.357(284)
06	1.67(0.01)	0.06(0.02)	0.434(0.003)	> 100	--(--)	--(--)	2845.1	--(--)	1.079(291)
07	1.68(0.01)	0.07(0.03)	0.444(0.004)	> 100	--(--)	--(--)	2870.2	--(--)	1.045(282)
08	1.76(0.01)	0.07(0.03)	0.393(0.003)	> 10	--(--)	--(--)	2366.8	--(--)	1.098(255)
09	1.8(0.01)	0.03(0.02)	0.383(0.003)	> 100	--(--)	--(--)	2302.1	--(--)	1.041(286)
10	1.79(0.01)	0.06(0.03)	0.384(0.003)	> 10	--(--)	--(--)	2259.2	--(--)	1.025(249)
<b><i>ObsId 00215769000 Date 6/23/2006 MJD 53909.671942</i></b>									
01	1.64(0.01)	0.05(0.02)	0.386(0.003)	> 100	--(--)	--(--)	2617.0	--(--)	1.099(310)
<b><i>ObsId 00030352015 Date 6/24/2006 MJD 53910.068887</i></b>									
01	1.83(0.01)	0.04(0.03)	0.447(0.004)	> 100	--(--)	--(--)	2601.0	--(--)	1.103(252)
02	1.85(0.01)	0.02(0.03)	0.409(0.003)	> 100	--(--)	--(--)	2367.8	--(--)	1.206(263)
03	1.85(0.01)	0.04(0.03)	0.406(0.003)	> 10	--(--)	--(--)	2323.1	--(--)	1.157(263)
04	1.83(0.01)	0.07(0.03)	0.418(0.003)	> 10	--(--)	--(--)	2389.7	--(--)	1.229(259)
05	1.84(0.01)	0.1(0.02)	0.439(0.003)	6(4)	$6^{+4}_{-2}$	816(22)	2440.4	1.76(0.05)	1.071(271)
06	1.78(0.01)	0.12(0.03)	0.473(0.004)	9(7)	$9^{+7}_{-3}$	957(40)	2707.7	2.06(0.09)	1.454(255)
07	1.78(0.01)	0.1(0.03)	0.478(0.004)	> 10	$12^{+15}_{-5}$	1009(61)	2775.9	2.2(0.1)	1.300(252)
08	1.78(0.01)	0.13(0.03)	0.485(0.004)	7(5)	$7^{+5}_{-2}$	968(35)	2766.7	2.08(0.07)	1.399(251)
09	1.87(0.01)	0.1(0.03)	0.455(0.004)	4(3)	$4^{+2}_{-1}$	800(14)	2467.9	1.72(0.03)	1.054(259)
10	1.9(0.01)	0.08(0.03)	0.458(0.004)	4(3)	$3.7^{+3}_{-0.9}$	780(13)	2454.4	1.68(0.03)	1.033(242)
11	1.92(0.01)	0.09(0.03)	0.402(0.003)	3(2)	$2.9^{+1}_{-0.5}$	670(7)	2128.7	1.44(0.01)	1.206(256)
12	1.93(0.01)	0.06(0.03)	0.376(0.003)	4(4)	$4^{+5}_{-1}$	630(11)	2009.5	1.36(0.02)	1.137(249)
13	1.92(0.01)	0.07(0.03)	0.359(0.003)	4(4)	$4^{+6}_{-1}$	609(13)	1926.6	1.31(0.03)	1.065(247)

(\*) gti with biased exposure, the affected data are not taken into account in the analyses.

The second third and fourth columns report the best fit estimate for the model in Eq. 2. The fifth column reports the value of the SED peak analytically estimated from Eq. 2 according to the best fit results. The sixth and seventh columns report the  $E_p$  and  $S_p$  best fit estimates using as best fit model Eq. 3. In the eighth column we report the flux in the 0.3–10.0 keV band, evaluated by Xspec integrating the Eq. 2 model. The ninth column reports the SED peak flux luminosity evaluated as  $L_p \simeq S_p 4\pi D_L^2$ , where  $D_L \simeq 134.1$  Mpc is the luminosity distance. In the last column we report the reduced  $\chi^2$  and the degrees of freedom concerning the Eq. 2 fit.

**Table 2.** *Swift*-XRT Spectral analysis of Mrk 421. *continued*

Orbit	$a$	$b$	K	$E_p^*$ keV	$E_p$ keV	$S_p$ $10^{-12} \text{ erg cm}^{-2} \text{ s}^{-1}$	flux 0.3-10 keV $10^{-12} \text{ erg cm}^{-2} \text{ s}^{-1}$	$L_p$ $10^{45} \text{ erg/s}$	$\chi_r^2/\text{dof}$
14	1.96(0.01)	0.06(0.03)	0.329(0.003)	2(1)	$2.1_{-0.4}^{+1}$	534(6)	1722.2	1.15(0.01)	1.277(236)
15	1.98(0.01)	0.1(0.03)	0.309(0.003)	1.3(0.3)	$1.3_{-0.2}^{+0.2}$	496(6)	1567.0	1.07(0.01)	1.135(212)
16	1.95(0.02)	0.08(0.04)	0.294(0.004)	2(1)	$2.1_{-0.4}^{+2}$	479(7)	1531.0	1.03(0.01)	1.305(162)
<b>ObsId 00030352016 Date 6/27/2006 MJD 53913.139963</b>									
01	1.99(0.01)	0(0.02)	0.253(0.002)	--	--(- -)	--(- -)	1350.6	--(- -)	1.001(261)
02	1.96(0.01)	-0(0.03)	0.243(0.002)	--	--(- -)	--(- -)	1324.9	--(- -)	1.079(247)
<b>ObsId 00219237000 Date 7/15/2006 MJD 53931.277331</b>									
01	1.65(0.02)	0.14(0.04)	0.509(0.007)	> 10	--(- -)	--(- -)	3193.8	--(- -)	1.048(171)
02	1.63(0.02)	0.17(0.04)	0.543(0.006)	13(11)	$13_{-4}^{+10}$	1393(105)	3406.2	3(0.2)	1.028(208)
03	1.66(0.02)	0.17(0.04)	0.534(0.006)	9(8)	$9_{-3}^{+7}$	1249(80)	3240.9	2.7(0.2)	0.979(191)
04	1.72(0.02)	0.13(0.04)	0.507(0.006)	> 10	$12_{-5}^{+16}$	1142(90)	3016.7	2.5(0.2)	1.009(191)
05	1.7(0.02)	0.18(0.04)	0.498(0.006)	6(4)	$6_{-2}^{+4}$	1050(44)	2906.0	2.26(0.09)	1.017(174)
06	1.66(0.02)	0.13(0.03)	0.48(0.005)	> 10	$19_{-8}^{+28}$	1275(134)	3008.1	2.7(0.3)	0.960(228)

(\*) gti with biased exposure, the affected data are not taken into account in the analyses.

The second third and fourth columns report the best fit estimate for the model in Eq. 2. The fifth column reports the value of the SED peak analytically estimated from Eq. 2 according to the best fit results. The sixth and seventh columns report the  $E_p$  and  $S_p$  best fit estimates using as best fit model Eq. 3. In the eighth column we report the flux in the 0.3-10.0 keV band, evaluated by Xspec integrating the Eq. 2 model. The ninth column reports the SED peak flux luminosity evaluated as  $L_p \simeq S_p 4\pi D_L^2$ , where  $D_L \simeq 134.1$  Mpc is the luminosity distance. In the last column we report the reduced  $\chi^2$  and the degrees of freedom concerning the Eq. 2 fit.

**Table 3.** *Swift*-*XRT* Orbit merged spectral analysis of Mrk 421.

Interval	$a$	$b$	$K$	$E_p^*$ keV	$E_p$ keV	$S_p$ $10^{-12} \text{ erg cm}^{-2} \text{ s}^{-1}$	flux 0.3-10 keV $10^{-12} \text{ erg cm}^{-2} \text{ s}^{-1}$	$L_p$ $10^{45} \text{ erg/s}$	$\chi^2/\text{dof}$
<b>ObsId 00206476000 Date 4/22/2006 MJD 53847.252792</b>									
01	1.68(0.009)	0.11(0.02)	0.349(0.002)	27(21)	$26_{-8}^{+19}$	941(60)	2181.3	2(0.1)	1.275(398)
<b>01 X+B</b>	1.68(0.01)	0.12(0.02)	0.351(0.002)		$20_{-6}^{+10}$				1.299(401)
02	1.76(0.01)	0.18(0.02)	0.289(0.002)	5(1)	$4.7_{-0.6}^{+1}$	558(9)	1620.6	1.2(0.02)	1.187(300)
03	1.8(0.01)	0.09(0.02)	0.26(0.002)	14(14)	$14_{-5}^{+15}$	540(27)	1499.0	1.16(0.06)	1.079(331)
04	1.79(0.01)	0.14(0.03)	0.257(0.002)	5(3)	$5_{-1}^{+2}$	488(11)	1434.8	1.05(0.02)	1.122(254)
05	1.804(0.009)	0.13(0.02)	0.281(0.002)	6(2)	$5.7_{-1}^{+2}$	532(9)	1570.4	1.14(0.02)	1.062(344)
<b>ObsId 00030352005 Date 4/25/2006 MJD 53850.267940</b>									
01	1.84(0.01)	0.15(0.02)	0.273(0.002)	3(1)	$3.3_{-0.4}^{+0.7}$	480(5)	1466.7	1.03(0.01)	1.350(288)
02	1.859(0.008)	0.16(0.02)	0.266(0.001)	2.8(0.5)	$2.8_{-0.2}^{+0.3}$	459(3)	1411.6	0.988(0.006)	1.363(379)
<b>ObsId 00030352006 Date 4/26/2006 MJD 53851.204919</b>									
01	1.824(0.009)	0.16(0.02)	0.289(0.002)	3.6(0.9)	$3.6_{-0.4}^{+0.6}$	519(5)	1570.7	1.12(0.01)	1.416(336)
<b>ObsId 00030352007 Date 4/26/2006 MJD 53851.951963</b>									
01	1.87(0.01)	0.16(0.03)	0.265(0.002)	2.6(0.6)	$2.6_{-0.3}^{+0.4}$	451(5)	1387.8	0.97(0.01)	1.085(258)
<b>ObsId 00030352008 Date 6/14/2006 MJD 53900.016100</b>									
01(c)	2.05(0.01)	0.15(0.03)	0.233(0.002)	0.67(0.1)	$0.7_{-0.1}^{+0.09}$	377(3)	1102.4	0.811(0.006)	1.108(333)
<b>ObsId 00030352009 Date 6/15/2006 MJD 53901.490493</b>									
01	1.86(0.01)	0.03(0.02)	0.17(0.001)	> 100	--(- -)	--(- -)	970.3	--(- -)	1.191(400)
02	1.87(0.01)	0.15(0.03)	0.191(0.001)	2.7(0.8)	$2.7_{-0.3}^{+0.5}$	326(3)	1007.0	0.701(0.006)	1.149(319)
<b>ObsId 00030352010 Date 6/16/2006 MJD 53902.025296</b>									
01	1.858(0.007)	0.1(0.01)	0.226(0.001)	6(2)	$6_{-1}^{+2}$	409(6)	1244.5	0.88(0.01)	1.297(413)
02	1.77(0.008)	0.07(0.01)	0.27(0.001)	> 10	--(- -)	--(- -)	1614.6	--(- -)	1.227(420)
03	1.713(0.008)	0.04(0.02)	0.3(0.001)	> 100	--(- -)	--(- -)	1927.8	--(- -)	1.268(423)
04	1.766(0.006)	0.04(0.01)	0.274(0.001)	> 100	--(- -)	--(- -)	1680.5	--(- -)	1.273(477)
05	1.823(0.007)	-0.02(0.01)	0.243(0.001)	--	--(- -)	--(- -)	1478.1	--(- -)	1.310(439)
06	1.748(0.008)	0.03(0.02)	0.294(0.001)	> 100	--(- -)	--(- -)	1840.3	--(- -)	1.320(414)
<b>ObsId 00030352011 Date 6/18/2006 MJD 53904.038766</b>									
01	1.808(0.009)	0.12(0.02)	0.319(0.002)	7(3)	$7_{-1}^{+3}$	613(13)	1794.7	1.32(0.03)	1.355(378)
02	1.82(0.01)	0.19(0.02)	0.341(0.002)	3(0.7)	$3_{-0.3}^{+0.4}$	600(6)	1814.2	1.29(0.01)	1.348(315)
03	1.932(0.008)	0.12(0.02)	0.293(0.002)	1.9(0.3)	$1.9_{-0.1}^{+0.2}$	479(3)	1508.2	1.031(0.006)	1.331(385)
04(c)	1.985(0.009)	0.09(0.02)	0.256(0.002)	1.2(0.2)	$1.2_{-0.1}^{+0.1}$	410(3)	1299.8	0.882(0.006)	1.115(325)
05	1.893(0.008)	0.07(0.02)	0.277(0.001)	6(4)	$6_{-1}^{+3}$	485(8)	1506.5	1.04(0.02)	1.209(395)
06	1.884(0.006)	0.08(0.01)	0.271(0.001)	5(2)	$5_{-0.9}^{+2}$	475(5)	1475.1	1.02(0.01)	1.253(473)
07	1.866(0.008)	0.05(0.02)	0.222(0.001)	> 10	--(- -)	--(- -)	1248.9	--(- -)	1.264(419)
08(c)	1.989(0.008)	0.09(0.02)	0.213(0.001)	1.2(0.1)	$1.2_{-0.1}^{+0.1}$	341(2)	1082.0	0.734(0.004)	1.148(392)
09	1.875(0.007)	0.01(0.01)	0.273(0.001)	> 100	--(- -)	--(- -)	1569.5	--(- -)	1.349(466)
10	1.821(0.007)	0.06(0.01)	0.298(0.001)	> 10	--(- -)	--(- -)	1720.5	--(- -)	1.295(467)
<b>ObsId 00030352012 Date 6/20/2006 MJD 53907.001774</b>									
01	1.842(0.007)	0.16(0.01)	0.289(0.001)	3.1(0.5)	$3.1_{-0.3}^{+0.3}$	506(3)	1545.3	1.089(0.006)	1.179(419)
02	1.871(0.008)	0.11(0.02)	0.228(0.001)	4(1)	$3.8_{-0.5}^{+0.5}$	398(4)	1230.8	0.856(0.009)	1.238(356)
03	1.861(0.008)	0.17(0.02)	0.287(0.001)	2.6(0.4)	$2.6_{-0.2}^{+0.2}$	491(3)	1509.5	1.056(0.006)	1.322(382)
04	1.857(0.009)	0.17(0.02)	0.331(0.002)	2.6(0.4)	$2.6_{-0.2}^{+0.2}$	568(4)	1741.4	1.222(0.009)	1.253(344)
05	1.915(0.009)	0.15(0.02)	0.318(0.002)	1.9(0.3)	$1.9_{-0.1}^{+0.1}$	522(4)	1623.3	1.123(0.009)	1.283(328)

(c) Orbit with a strong cooling contamination.

The second third and fourth column report the best fit estimate for the model in Eq. 2. The fifth column reports the value of the SED peak analytically estimated from Eq. 2 according to the best fit results. The sixth and seventh columns report the  $E_p$  and  $S_p$  best fit estimates using as best fit model Eq. 3. In the eighth column we report the flux in the 0.3-10.0 keV band, evaluated by X-spec integrating the Eq. 2 model. The ninth column reports the SED peak flux luminosity evaluated as  $L_p \approx S_p 4\pi D_L^2$ , where  $D_L \approx 134.1$  Mpc is the luminosity distance. In the last column we report the reduced  $\chi^2$  and the degrees of freedom concerning the Eq. 2 fit.

**Table 2.** *Swift*-XRT Orbit merged spectral analysis of Mrk 421. *continued*

Interval	$a$	$b$	$K$	$E_p^*$ keV	$E_p$ keV	$S_p$ $10^{-12} \text{ erg cm}^{-2} \text{ s}^{-1}$	flux 0.3-10 keV $10^{-12} \text{ erg cm}^{-2} \text{ s}^{-1}$	$L_p$ $10^{45} \text{ erg/s}$	$\chi_r^2/\text{dof}$
<b>ObsId 00030352013 Date 6/22/2006 MJD 53908.050644</b>									
01	1.942(0.007)	0.17(0.01)	0.3(0.001)	1.5(0.1)	$1.47^{+0.06}_{-0.05}$	485(3)	1493.6	1.044(0.006)	1.261(393)
02(c)	1.982(0.008)	0.12(0.02)	0.255(0.001)	1.18(0.1)	$1.18^{+0.07}_{-0.07}$	408(2)	1272.0	0.878(0.004)	1.247(354)
03	1.93(0.01)	0.04(0.03)	0.243(0.002)	> 10	--(- -)	--(- -)	1323.0	--(- -)	1.119(244)
04	1.81(0.01)	0.03(0.02)	0.281(0.002)	> 100	--(- -)	--(- -)	1665.7	--(- -)	1.403(278)
05	1.805(0.009)	0.09(0.02)	0.251(0.001)	14(12)	$14^{+13}_{-5}$	520(23)	1446.2	1.12(0.05)	1.268(351)
06	1.87(0.006)	0.02(0.01)	0.242(0.001)	> 100	--(- -)	--(- -)	1380.5	--(- -)	1.263(455)
<b>ObsId 00030352014 Date 6/23/2006 MJD 53909.394900</b>									
01	1.74(0.01)	0.02(0.02)	0.326(0.003)	> 100	--(- -)	--(- -)	2060.1	--(- -)	1.163(281)
02	1.67(0.01)	0.06(0.03)	0.372(0.003)	> 100	--(- -)	--(- -)	2435.1	--(- -)	1.240(255)
03	1.66(0.01)	0.02(0.03)	0.411(0.004)	> 100	--(- -)	--(- -)	2783.6	--(- -)	1.110(276)
04	1.69(0.01)	0.04(0.03)	0.398(0.003)	> 100	--(- -)	--(- -)	2603.6	--(- -)	1.234(265)
05	1.63(0.01)	0.08(0.03)	0.436(0.004)	> 100	--(- -)	--(- -)	2938.2	--(- -)	1.357(284)
<b>05 X+B</b>	1.61(0.01)	0.13(0.02)	0.434(0.004)		$34^{+22}_{-11}$				1.399(287)
06	1.67(0.01)	0.06(0.02)	0.434(0.003)	> 100	--(- -)	--(- -)	2845.1	--(- -)	1.079(291)
07	1.68(0.01)	0.07(0.03)	0.444(0.004)	> 100	--(- -)	--(- -)	2870.2	--(- -)	1.045(282)
08	1.76(0.01)	0.07(0.03)	0.393(0.003)	> 10	--(- -)	--(- -)	2366.8	--(- -)	1.098(255)
09	1.8(0.01)	0.03(0.02)	0.383(0.003)	> 100	--(- -)	--(- -)	2302.1	--(- -)	1.041(286)
10	1.79(0.01)	0.06(0.03)	0.384(0.003)	> 10	--(- -)	--(- -)	2259.2	--(- -)	1.025(249)
<b>ObsId 00215769000 Date 6/23/2006 MJD 53909.671942</b>									
01	1.64(0.01)	0.05(0.02)	0.386(0.003)	> 100	--(- -)	--(- -)	2617.0	--(- -)	1.099(310)
<b>ObsId 00030352015 Date 6/24/2006 MJD 53910.068887</b>									
01	1.844(0.007)	0.04(0.01)	0.422(0.002)	> 100	--(- -)	--(- -)	2434.7	--(- -)	1.317(418)
02	1.778(0.008)	0.12(0.02)	0.479(0.002)	8(4)	$8^{+3}_{-2}$	970(22)	2752.4	2.09(0.05)	1.474(399)
03	1.832(0.009)	0.09(0.02)	0.43(0.002)	9(7)	$9^{+6}_{-3}$	829(24)	2422.2	1.78(0.05)	1.181(354)
04	1.907(0.005)	0.08(0.01)	0.398(0.001)	4(1)	$3.6^{+0.7}_{-0.4}$	675(4)	2131.8	1.452(0.009)	1.259(482)
05(c)	1.964(0.009)	0.08(0.02)	0.313(0.002)	1.7(0.4)	$1.7^{+0.2}_{-0.2}$	505(3)	1618.7	1.087(0.006)	1.367(322)
<b>ObsId 00030352016 Date 6/27/2006 MJD 53913.139963</b>									
01	1.973(0.008)	0(0.02)	0.248(0.001)	--	--(- -)	--(- -)	1338.5	--(- -)	1.072(339)
<b>ObsId 00219237000 Date 7/15/2006 MJD 53931.277331</b>									
01	1.65(0.01)	0.17(0.02)	0.532(0.004)	11(5)	$11^{+4}_{-2}$	1299(50)	3288.2	2.8(0.1)	1.147(322)
<b>01 X+B</b>	1.64(0.01)	0.20(0.02)	0.535(0.05)		$8^{+2}_{-1}$				1.235(325)
02	1.684(0.009)	0.16(0.02)	0.504(0.003)	9(4)	$9^{+3}_{-2}$	1150(32)	3035.6	2.47(0.07)	1.136(369)

(c) Orbit with a strong cooling contamination.

The second third and fourth column report the best fit estimate for the model in Eq. 2. The fifth column reports the value of the SED peak analytically estimated from Eq. 2 according to the best fit results. The sixth and seventh columns report the  $E_p$  and  $S_p$  best fit estimates using as best fit model Eq. 3. In the eighth column we report the flux in the 0.3-10.0 keV band, evaluated by X-spec integrating the Eq. 2 model. The ninth column reports the SED peak flux luminosity evaluated as  $L_p \approx S_p 4\pi D_L^2$ , where  $D_L \approx 134.1$  Mpc is the luminosity distance. In the last column we report the reduced  $\chi^2$  and the degrees of freedom concerning the Eq. 2 fit.



## References

- Achterberg, A., Gallant, Y. A., Kirk, J. G., & Guthmann, A. W. 2001, *MNRAS*, 328, 393
- Aharonian, F., Akhperjanian, A. G., Bazer-Bachi, A. R., et al. 2006, *Nature*, 440, 1018
- Albert, J., Aliu, E., Anderhub, H., et al. 2006, *ApJ*, 642, L119
- Albert, J., Aliu, E., Anderhub, H., et al. 2007, *ApJ*, 663, 125
- Becker, P. A., Le, T., & Dermer, C. D. 2006, *ApJ*, 647, 539
- Bednarek, W. & Protheroe, R. J. 1999, *MNRAS*, 310, 577
- Blasi, P. & Vietri, M. 2005, *ApJ*, 626, 877
- Burrows, D. N., Hill, J. E., Nousek, J. A., et al. 2005, *Space Science Reviews*, 120, 165
- Ellison, D. C. & Double, G. P. 2004, *Astroparticle Physics*, 22, 323
- Falcone, A. D., Cui, W., & Finley, J. P. 2004, *ApJ*, 601, 165
- Fitzpatrick, E. L. 1999, *PASP*, 111, 63
- Fossati, G., Celotti, A., Chiaberge, M., et al. 2000a, *ApJ*, 541, 153
- Fossati, G., Celotti, A., Chiaberge, M., et al. 2000b, *ApJ*, 541, 166
- Gallant, Y. A., Achterberg, A., & Kirk, J. G. 1999, *A&AS*, 138, 549
- Ghisellini, G. & Maraschi, L. 1989, *ApJ*, 340, 181
- Giebels, B., Dubus, G., & Khélifi, B. 2007, *A&A*, 462, 29
- Hill, J. E., Burrows, D. N., Nousek, J. A., et al. 2004, in *Presented at the Society of Photo-Optical Instrumentation Engineers (SPIE) Conference, Vol. 5165, X-Ray and Gamma-Ray Instrumentation for Astronomy XIII*. Edited by Flanagan, Kathryn A.; Siegmund, Oswald H. W. *Proceedings of the SPIE, Volume 5165*, pp. 217–231 (2004).., ed. K. A. Flanagan & O. H. W. Siegmund, 217–231
- Jones, T. W., O'dell, S. L., & Stein, W. A. 1974, *ApJ*, 188, 353
- Kardashev, N. S. 1962, *Soviet Astronomy*, 6, 317
- Kataoka, J., Takahashi, T., Makino, F., et al. 2000, *ApJ*, 528, 243
- Katarzyński, K., Ghisellini, G., Mastichiadis, A., Tavecchio, F., & Maraschi, L. 2006, *A&A*, 453, 47
- Kino, M., Takahara, F., & Kusunose, M. 2002, *ApJ*, 564, 97
- Kirk, J. G., Rieger, F. M., & Mastichiadis, A. 1998, *A&A*, 333, 452
- Lemoine, M. & Pelletier, G. 2003, *ApJ*, 589, L73
- Li, W., J. S. F. A. B. J. e. a. 2006, *SSRv*, 120, 143
- Lichti, G. G., Bottacini, E., Ajello, M., et al. 2008, *ArXiv e-prints*, 805
- Lin, Y. C., Bertsch, D. L., Chiang, J., et al. 1992, *ApJ*, 401, L61
- Lockman, F. J. & Savage, B. D. 1995, *ApJS*, 97, 1
- Massaro, E., Perri, M., Giommi, P., Nesci, R., & Verrecchia, F. 2004, *A&A*, 422, 103
- Massaro, E., Tramacere, A., Perri, M., Giommi, P., & Tosti, G. 2006, *A&A*, 448, 861
- Massaro, F., Tramacere, A., Cavaliere, A., Perri, M., & Giommi, P. 2008, *A&A*, 478, 395
- Mészáros, P. 2002, *ARA&A*, 40, 137
- Padovani, P. & Giommi, P. 1995, *MNRAS*, 277, 1477
- Park, B. T. & Petrosian, V. 1995, *ApJ*, 446, 699
- Petry, D., Bradbury, S. M., Konopelko, A., et al. 1996, *A&A*, 311, L13
- Punch, M., Akerlof, C. W., Cawley, M. F., et al. 1992, *Nature*, 358, 477
- Roming, P. W. A., K. T. E. M. K. O. e. a. 2005, *SSRv*, 120, 143
- Rybicki, G. B. & Lightman, A. P. 1979, *Radiative processes in astrophysics* (New York, Wiley-Interscience, 1979. 393 p.)
- Sato, R., Kataoka, J., Takahashi, T., et al. 2008, *ApJ*, 680, L9
- Schlegel, D. J., Finkbeiner, D. P., & Davis, M. 1998, *ApJ*, 500, 525
- Spitkovsky, A. 2008, *ApJ*, 682, L5
- Stawarz, L. & Petrosian, V. 2008, *ArXiv e-prints*, 803
- Takahashi, T., Tashiro, M., Madejski, G., et al. 1996, *ApJ*, 470, L89+
- Tanihata, C., Kataoka, J., Takahashi, T., & Madejski, G. M. 2004, *ApJ*, 601, 759
- Tanihata, C., Urry, C. M., Takahashi, T., et al. 2001, *ApJ*, 563, 569
- Tavecchio, F., Maraschi, L., & Ghisellini, G. 1998, *ApJ*, 509, 608
- Tramacere, A. 2007, PhD thesis, “Spectral Variability in Blazar’s High Energy Emission “ La Sapienza University, Rome (2007)
- Tramacere, A. 2009, in preparation
- Tramacere, A., Giommi, P., Massaro, E., et al. 2007a, *A&A*, 467, 501
- Tramacere, A., Massaro, F., & Cavaliere, A. 2007b, *A&A*, 466, 521
- Urry, C. M., Scarpa, R., O’Dowd, M., et al. 2000, *ApJ*, 532, 816
- Waxman, E. 1997, *ApJ*, 485, L5+
- Yadav, K. K., Chandra, P., Tickoo, A. K., et al. 2007, *Astroparticle Physics*, 27, 447
- Zhang, Y. H. 2002, *MNRAS*, 337, 609